1   **Carbonate clumped isotope values compromised by nitrate-derived NO₂ interferent**

2

3   Jens Fiebig[1]*, Miguel Bernecker[1], Niels Meijer[2], Katharina Methner[3], Philip Staudigel[1],

4   Amelia Jane Davies[1], Lkhamsuren Bayarjargal[1], Dominik Spahr[1], Björn Winkler[1]

5

6   [1]Institute of Geosciences, Goethe University Frankfurt, Altenhöferallee 1, 60438 Frankfurt,

7   Germany

8   [2]Senckenberg Biodiversity and Climate Research Centre (SBiK-F), Senckenberganlage 25,

9   60325 Frankfurt, Germany

10   [3]Institute for Earth System Science and Remote Sensing, University of Leipzig, Talstrasse 35,

11   04103 Leipzig, Germany

12

13   *corresponding author; email: Jens.Fiebig@em.uni-frankfurt.de

14

15   **Abstract**

16   Δ_{47} based clumped isotope thermometry has enabled reconstruction of Earth's surface

17   temperatures independent of the source of oxygen within the carbonate. It has been postulated

18   that carbonate samples can contain contaminants that cause isobaric interferences,

19   compromising measured Δ_{47} values and reconstructed temperatures. The exact nature of

20   contaminants and isobaric interferents, however, largely remained unidentified.

21   Here, we demonstrate that compromised measurements can be identified through high-

22   precision analysis of Δ_{48} alongside Δ_{47}. We provide evidence that nitrate constitutes a serious

23   contaminant even if present in the carbonate in sub-wt-% quantities only. During phosphoric

24   acid digestion of carbonates at 90°C, nitrate decomposes to NO_2, which, in turn, is not

25   effectively removed during subsequent purification of carbonate-derived CO_2 using cryogenic

26   traps and gas chromatography (packed Porapak Q column at -15°C). In dual clumped isotope

27   space, samples affected by variable sub-ppm contributions of NO_2 to CO_2 plot along a

28   characteristic slope of -0.3, in agreement with theoretical predictions. Nitrate contamination

29   occurs in a synthetic calcite precipitated using $Ca(NO_3)_2$, a pedogenic carbonate nodule, a

30   plasma-ashed echinoid spine, ETH-3 (a recently assigned anchor for Δ_{47} analysis of carbonates)

31   and, presumably, in a bioapatite (Greenland shark dentine). The extent of NO_2 generation may

32   depend on analytical setup and additional parameters such as nitrate concentration inside the

33   carbonate, acid digestion temperature, reaction time, filament current and filament age.

34 Sequential bleaching tests reveal that nitrate contaminant can be effectively removed from
35 carbonates if samples are pre-treated overnight with 3 wt-% sodium hypochlorite (NaOCl).
36 Our high-precision long-term Δ_{47} (CDES 90) values for ETH-1 and ETH-2 (Bernecker et al.,
37 2023) and for bleached ETH-3 exactly confirm recently assigned Δ_{47}-I-CDES values for these
38 standards. Unless independent evidence is given that NO_2 contamination is irrelevant for a
39 specific analytical setup we strongly recommend that ETH-3 is bleached with 3 wt-% NaOCl
40 overnight in order to enable accurate projection of raw data to the I-CDES. Moreover,
41 systematic bleaching tests should be carried out on unknown samples in order to avoid any
42 isotopic bias.

43

44 **1 Introduction**

45 Carbonate clumped isotope thermometry represents a well-established method to reconstruct
46 carbonate formation temperature independent of the isotopic composition of the water the
47 mineral crystallized from (Ghosh et al., 2006; Eiler et al., 2011). Its temperature dependence is
48 expressed by the Δ_{47} value which quantifies the extent to which the internal distribution of
49 heavy carbon and oxygen isotopes amongst carbonate isotopologues with cardinal mass 63
50 departs from stochastic partitioning, as predicted by the given bulk carbon and oxygen isotopic
51 composition of the carbonate. Since excess abundance measurements of ^{13}C-^{18}O isotopologues
52 of cardinal mass 63 cannot be carried out on the carbonate directly, these measurements are
53 performed on CO_2 that is extracted from the carbonate by reacting it quantitatively with
54 phosphoric acid (Ghosh et al., 2006). Due to the relatively low average natural abundance of
55 ^{13}C-^{18}O bearing CO_2 isotopologues of mass 47 of ca. 45 ppm and the low mass resolution of
56 most gas source mass spectrometers, Δ_{47} analyses can be easily compromised by non-CO_2
57 isotopologues which occur isobaric to m/z 47 (e.g., Eiler & Schauble, 2004; Huntington et al.,
58 2009; Eagle et al., 2010; Bergmann et al., 2018). Eiler & Schauble (2004) noticed that N_2O,
59 hydrocarbons and chlorinated hydrocarbons cause serious isobaric bias during Δ_{47} analyses of
60 atmospheric CO_2 samples. Whereas hydrocarbons and chlorinated hydrocarbons could be
61 effectively removed by exposing the analyte CO_2 to UV-radiation and cryogenic traps, the bias
62 arising from N_2O contamination required an empirical correction approach taking into account
63 additional analysis of well-defined CO_2-N_2O mixtures and N/C ratios specific of samples and
64 mixtures. On the contrary, for carbonates subjected to phosphoric acid digestion, the origin of
65 isobaric contamination has been poorly investigated. Identification of samples apparently
66 unbiased by isobaric m/z contaminants relied on the application of ambiguous criteria from
67 which it often remained open if sample-Δ_{47} was affected at all. The most widely applied is the

extent to which the excess abundance of apparent m/z 48 CO_2 isotopologues in carbonate-derived CO_2 (expressed as Δ_{48} value) deviates from that in equilibrated gas standards (Huntington et al., 2009). This approach assumes that the contaminant contributing to m/z 47 also contributes to m/z 48, an assumption that is not necessarily true. For example, SO contaminant will just cause isobaric interference on m/z 48, but not on m/z 47. Moreover, m/z 48 based approaches to identify samples with compromised Δ_{47} often rely on arbitrarily or statistically set threshold values for Δ_{48} (e.g., Passey et al., 2010; Snell et al., 2014; Davies & John, 2017; Staudigel et al., 2018) from which the relevance and extent of isobaric contamination on m/z 47 remains unconstrained. It has been demonstrated that secondary electrons originating from the interaction of the major m/z 44 ion-beam with the flight tube, electromagnet, or Faraday collectors, also contribute to measured m/z 47 and 48 intensities, shifting the baseline below m/z 47 and 48 Faraday cups into the negative range (He et al., 2012; Bernasconi et al., 2013; Fiebig et al., 2016). If unaccounted for, this negative pressure baseline (PBL) effect results in biases that scale inversely with the natural abundance of m/z 47 and 48 CO_2 isotopologues, such that the bias in Δ_{48} roughly exceeds that in Δ_{47} values by one order of magnitude (Wacker et al., 2016; Bernecker et al., 2023). In this respect, uncommon Δ_{48} values are not unambiguously diagnostic of isobaric interferences on m/z 47 either, especially when no PBL correction of measured raw m/z 47 and 48 intensities has been performed.

The latest generation of gas source mass spectrometers benefits from an improved setup that matches the requirements for more precise simultaneous detection of CO_2 isotopologues whose abundances vary by 5 to 6 orders of magnitude. With the introduction of the 253plus gas source mass spectrometer, the generation and collection of secondary electrons has been reduced, the signal to noise ratio of amplifiers improved and continuous monitoring of the negative PBL below m/z 47 and 48 made possible (e.g., Fiebig et al., 2019). With these improvements, long-term Δ_{47} and Δ_{48} analyses with precisions very close to mass spectrometric shot-noise level have now become available (Bernecker et al., 2023). Highest-precision dual clumped isotope thermometry allows researchers to resolve the extent to which the bulk stable and clumped isotope compositions of a pristine carbonate were affected by kinetic limitations in addition to temperature (Fiebig et al., 2019; Guo & Zhou, 2019; Guo, 2020; Bajnai et al., 2020). Moreover, temperature can be accurately isolated from the kinetic information based on measured Δ_{47} and Δ_{48} values alone (Bajnai et al., 2020; Fiebig et al., 2021; Davies et al., 2022, 2023; Tagliavento et al., 2023a). In addition, it has become possible to reconstruct peak-diagenetic temperatures from dual clumped analysis of partially altered samples (Staudigel et al., 2023a, Staudigel et al., 2023b). Here, we show that combined high-precision analysis of Δ_{47} and Δ_{48} also helps to

102 identify the presence and origin of isobaric contaminants in natural carbonate samples. We

103 demonstrate that the presence of trace amounts of nitrate in a given carbonate sample leads to

104 compromised Δ_{47} and Δ_{48} values. We also show that, following our methods of CO_2 preparation

105 and purification, the presence of pyrite does not affect Δ_{48} values. Nitrate can be effectively

106 removed from the sample by pre-treatment with 3 wt-% NaOCl overnight.

107

108 **2 Methods**

109 **2.1 Samples**

110 Dual clumped isotope analyses were performed on pedogenic carbonates, ETH-3, a synthetic

111 calcite, an echinoid spine, Greenland shark dentine, carbonate skeletons from brachiopods,

112 warm- and cold-water corals, and on authigenic methane seep carbonates:

113 Pedogenic carbonate samples were directly prepared from untreated nodules using mortar and

114 pestle. HGB-42a represents a pedogenic nodule from Hell Gate Basin located in the Miocene

115 Barstow Formation, Mud Hills, California, USA (Loughney & Badgley, 2017). Samples HGB-

116 42a$_{NEW}$ and HGB-42a$_{NEWEST}$ represent newly prepared aliquots from the same nodule.

117 BW-33.7 is a calcite that has been precipitated at a temperature of 33.7°C through slow and

118 dropwise addition of a $Ca(NO_3)_2$ solution to a $NaHCO_3$ solution (Spahr et al., 2021). Analytical-

119 grade calcium nitrate tetrahydrate $Ca(NO_3)_2 * 4 H_2O$ (99.95 % purity, Merck KGaA,

120 Darmstadt, Germany) and sodium bicarbonate $NaHCO_3$ ($\geq$ 99.7 % purity, Merck KGaA,

121 Darmstadt, Germany) were dissolved separately in bi-distilled water in two 5-liter laboratory

122 bottles, to obtain solutions with a concentration of 10 mmol/L. Both glass vessels were sealed

123 gas-tight and connected to each other by a transfer tube for the solution and a compensation

124 line. Afterwards, the glass bottles were equilibrated in an air thermostat while the solutions

125 were continuously stirred. After reaching the target temperature of 33.7°C in the solutions, they

126 were kept for seven days in the thermostat before the precipitation was started in order to

127 achieve full isotopic equilibration between dissolved inorganic carbon species and water.

128 Temperature was controlled using a Julabo LC6 temperature controller with a temperature

129 stability of ±0.03°C. Precipitation was initiated by slowly ($\approx$ 10 mL/h) adding the calcium

130 nitrate solution to the sodium bicarbonate solution using a VWR PP1080 peristaltic pump while

131 magnetic stirring. Precipitated $CaCO_3$ was separated from its parent solution by vacuum

132 filtration. Raman analysis revealed that the precipitated $CaCO_3$ was pure calcite (Fig. 1).

133 Sample SD-MAI-S has been made available from spines of *Stronglyocentrotus Droebachiensis*.

134 This echinoid specimen has been hatched in an aquaculture facility at the University of Maine

135 at a temperature of 8.5°C. Spines collected from this specimen have been ground to powder

using mortar and pestle. An aliquot of the ground and homogenized powder (SD-MAI-S2) was treated by low temperature plasma ashing under oxygen at a flow rate of 400 ml/min for at least 30 minutes in order to remove organic matter as CO_2 (Davies & John, 2018).

Samples LP-SM (*Desmophyllum Pertusum*), A4 (*Acropora cervicornis*) and A6 (*Acropora sp.*) are cold- and warm-water corals, respectively. These aragonitic samples were described in more detail in Davies et al. (2022). KASU_NOT and KIWI_INC are calcitic eggshells of a Cassowary and a Kiwi, respectively (Tagliavento et al., 2023a). MV130b and MBHB represent new aliquots from Brachiopod shells of species *Magellania venosa* and *Hemithiris psittacea*, respectively, previously sampled for dual clumped isotope investigations by Davies et al. (2023). Carb2A (aragonite) and Carb3C (calcite) (DIVE ID's 54-2 and 61-2, respectively) are authigenic methane seep carbonates from Formosa Ridge previously described and analyzed for their dual clumped isotope composition by Staudigel et al. (2024).

ETH-3 represents Cretaceous chalk from the Isle of Rügen, Germany, which is – along with ETH-1 and ETH-2 – used as a low-temperature anchor for standardization of mass spectrometric Δ_{47} raw data obtained on carbonate unknowns (Bernasconi et al., 2021).

Finally, we also analyzed carbonate-bearing dentine from a Greenland Shark (sample SLGDenA). This sample was prepared as described in Löffler et al. (2019).

2.2 Bleaching of samples

With the exception of SD-MAI-S, SD-MAI-S2 and SLGDenA, bleached aliquots (suffix OXI) were prepared from each sample and analyzed along with their unbleached aliquots. Samples were treated with 3 wt-% sodium-hypochlorite (NaOCl) and left to react overnight (at least 8 hours). Afterwards, the samples were rinsed by adding demineralized water, thoroughly mixing the solution and sample, centrifuging and decanting the solution. This rinsing step was repeated 4 times in total. The samples were subsequently dried in a vacuum oven at 30°C.

Given aliquots of HGB-42a and ETH-3 were treated twice with 3 wt-% NaOCl (suffix OXI2) in order to test the effect of sequential bleaching steps on the bulk and clumped isotopic composition. In addition, a new aliquot of ETH-3 was bleached once again (suffix NEW, OXI) in order to test the reproducibility of bleaching and its effect on the isotopic composition. From HGB-42a a third aliquot (suffix RINSE) was treated exactly the same way as described above, but with de-ionized water instead of 3 wt-% NaOCl.

2.3 Dual clumped isotope analysis

Replicate aliquots corresponding to 10 mg of pure $CaCO_3$ were weighed into silver capsules and stored in a vacuum oven at 30°C until analysis. For isotopic analysis, the capsules were

loaded into the low-blank autosampler of the automated gas preparation line HAL, which is connected to the dual inlet system of a 253plus gas source mass spectrometer (Fiebig et al., 2019). With the exception of SLGDenA, which was reacted for 90 minutes, all samples were digested with 108-109 wt-% phosphoric acid for 30 minutes. Some samples were additionally reacted in quartz capsules (suffix QZ). Whenever samples were reacted in quartz capsules no silver capsules were present in the acid. The evolved CO_2 was purified using four cryogenic traps (-80°C) and gas chromatography (packed Porapak Q column, 80-100 mesh, at -15°C), as detailed in Fiebig et al. (2019). The purified CO_2 was finally analyzed for its dual clumped isotope composition at an m/z 44 intensity of 16 Volts in 13 acquisitions consisting of 10 cycles each (20 seconds integration time per cycle). Mass spectrometric m/z 47-49 raw intensities were corrected for a negative PBL effect using a m/z 47.5 half mass cup, and Δ_{47} and Δ_{48} values are finally reported on the CDES 90. Preparation of equilibrated gases, PBL correction and data normalization has been described in detail by Bernecker et al. (2023). Unless indicated otherwise, all PBL corrected data was evaluated in the pooled approach using D47crunch (Daëron, 2021), considering variance minimization of anchors and samples over all sessions for the determination of session-specific correction parameters a, b and c (MSP approach, Bernecker et al., 2023). Treating data this way allows for a better correction of drifts that may occur between and within single sessions, e.g., through temporal variations in the phosphoric acid reaction environment (Daëron, 2021). However, as we show in Section 4.1, our analytical setup yields Δ_{47} and Δ_{48} values for ETH-3 that are compromised by the presence of isobaric non-CO_2 interferent. Since ETH-3 makes up a significant fraction of all measured data (ca. 8 %), carbonate anchor ETH-3 was, therefore, excluded from variance minimization in the MSP approach. This can be easily achieved providing individual identifiers for each unbleached ETH-3 replicate. Since bleached ETH-3 aliquots were not suffering from contamination anymore (see Section 4.3), it was pooled over all bleached replicates in this approach.

In the last session, we tested the effect of reaction time and sequential NaOCl pre-treatment on the dual clumped isotope composition of ETH-3. In addition to the MSP approach described above, this session was evaluated separately in two more modes: 1) treating unbleached ETH-3 (ETH-3), once bleached ETH-3 (ETH-3$_{OXI}$), twice bleached ETH-3 (ETH-3$_{OXI2}$), newly bleached ETH-3 (ETH-3$_{NEW, OXI}$) and unbleached ETH-3 reacted for 10 minutes (ETH-3$_{10min}$) as individual samples, while anchoring all raw data against nominal values of equilibrated gases both for Δ_{47}, Δ_{48} and Δ_{49} (Bernecker et al., 2023) (see Section 4.3); 2) pooling over all bleached ETH-3 replicates (n = 34) while anchoring raw data against nominal values of equilibrated

204 gases and ETH-1 and ETH-2 for Δ_{47} exclusively (see Section 4.8). Again, individual identifiers

205 were used for each unbleached ETH-3 replicate in these two additional approaches.

206 Mass spectrometric shot noise limit (total counting time of 2600 seconds per replicate at an m/z

207 44 intensity of 16 Volts) is 7.0 ppm and 23.4 ppm for Δ_{47} and Δ_{48}, respectively.

208 D47crunch also provides the option to normalize $\delta^{13}C_{VPDB}$ and $\delta^{18}O_{VPDB}$ data of unknown

209 samples relative to ETH carbonate standards (Daëron, 2021). For this purpose, we have

210 considered the nominal $\delta^{13}C_{VPDB}$ and $\delta^{18}O_{VPDB}$ values of ETH-1 and ETH-2 reported by

211 Bernasconi et al. (2018).

212

213 **2.4 Raman spectroscopy**

214 Raman measurements were carried out with a custom set-up in Frankfurt described in detail

215 elsewhere (Bayarjargal et al., 2018). We used an OXXIUS S.A. Laser-Boxx LMX532 laser

216 (λ = 532 nm) and a spectrograph (Princeton Instruments ACTON SpectraPro 2300i) equipped

217 with a Pixis256E CCD camera. Measurements were performed in reflection geometry with the

218 polarized laser light. The spectral resolution of our spectrometer is 3 cm^{-1} and the accuracy is

219 around 0.5 cm^{-1}. Raman measurements were performed with an exposure time of 5-30 sec and

220 with a power of 8-26 mW. Raman spectra were acquired on three samples: (I) a transparent

221 large single calcite crystal, (II) BW-33.7 and (III) SD-MAI-S2.
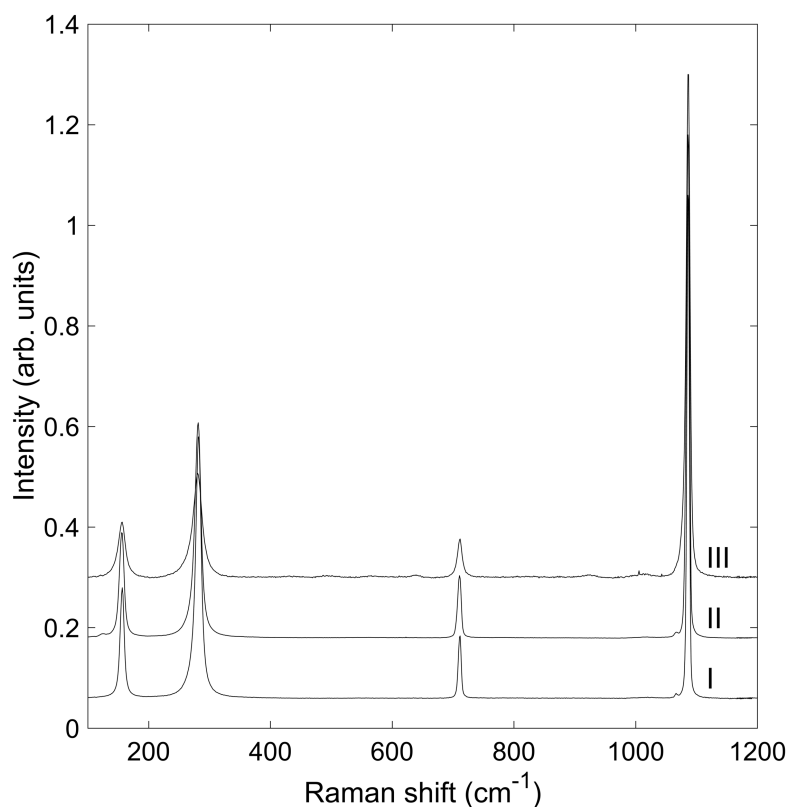
222

223 **Fig. 1.** Raman spectra of samples I (single calcite crystal), II (BW-33.7) and III (SD-MAI-S2). For further discussion see
224 Section 4.2.

2.5 Modeling of isotopic bias introduced by isobaric interferents

The presence of contaminants being isobaric to CO_2 will bias $\delta^{13}C$, $\delta^{18}O$, Δ_{47} and Δ_{48} values of carbonate-derived CO_2 along vectors which are characteristic of the chemical and isotopic composition of the contaminant. Supplementary Table S1 presents an excel sheet ("isobaric interference calculator") that computes how isobaric contamination with SO^+, N_2O^+, NO_2^+, CH_3S^+, CS^+ and CCl^+ will affect $\delta^{13}C$, $\delta^{18}O$, Δ_{47} and Δ_{48} values of CO_2. This calculator considers H, N, S and Cl isotopic compositions of interfering gases relative to VSMOW, V-Air-N_2, VCDT and SMOC respectively, whereas C and O isotope compositions of analyte CO_2 and interferents are provided relative to the VPDB-CO_2 scale. In a first step, the abundances of m/z 44-49 isotopologues in the mixture made up of CO_2 and interferent are calculated assuming random distribution of all isotopes amongst interfering isotopologues. In a next step, apparent $\delta^{13}C$-CO_2 and $\delta^{18}O$-CO_2 values are calculated from 45/44 and 46/44 abundance ratios characteristic of the mixture, as outlined for pure CO_2 by Brand et al. (2010). In a final step, apparent Δ_{47}, Δ_{48} and Δ_{49} values of the mixture are calculated from corresponding 47/44, 48/44 and 49/44 isotopologue ratios and apparent stochastic values computed from apparent $\delta^{13}C$-CO_2 and $\delta^{18}O$-CO_2 values.

3 Results

3.1 Contamination vectors in Δ_{47} - Δ_{48} and Δ_{48} - Δ_{49} space

Δ_{47} - Δ_{48} vectors theoretically predicted for relatively small contributions of NO_2, N_2O, SO, CCl, CS and CH_3S to analyte CO_2 are shown in Figure 2a, assuming the analyte CO_2 has bulk and clumped isotopic composition corresponding to VPDB-CO_2 and stochastically predicted values of zero, respectively. It can be easily shown using our isobaric interference calculator (Supplementary Table S1) that the clumped isotope composition of the analyte CO_2 has no significant effect on the extent of interferent-specific isotopic bias. For interferents without m/z 44-46 isotopologues (SO, CH_3S, CCl) contamination vectors represent linear mixing lines over the entire range of relative contributions of analyte CO_2 and interferent. For NO_2 and CS the slope of the mixing vector remains constant within three digits (and, hence, can be approached linearly) if these interferents make up less than 1 ppm (NO_2) and 100 ppm (CS) of the total gas mixture.

Δ_{47} and Δ_{48} values are very sensitive to contamination from NO_2. A contribution of 40 ppb of NO_2 to CO_2 would already result in an isotopic bias of -6 ppm and 19 ppm in Δ_{47} and Δ_{48}, respectively, closely corresponding to the average lower and upper boundary of our fully

259 propagated 2 SE for Δ_{47} and Δ_{48} analysis. This bias increases to -72 ppm in Δ_{47} and to 240 ppm

260 in Δ_{48}, if the molar fractional abundance of NO_2 increases to 500 ppb. Within this range, the

261 slope of the corresponding contaminant vector is -0.30, and relatively insensitive to natural

262 variations in the abundances of C, N and O isotopes in the contaminant NO_2 and analyte CO_2.

263 For example, if, within the above range of NO_2 contribution, $\delta^{15}N$ and $\delta^{18}O$ are varied by ± 50

264 ‰, this will only make the slope of the vector change by $\leq \pm 0.01$ and ± 0.04, respectively. An

265 additional variation of ± 0.04 in this slope can be introduced through carbon and oxygen isotope

266 variations in the analyte CO_2. Of all contaminants investigated in this study, NO_2 is the only

267 one that introduces a paired $-\Delta_{47}/+\Delta_{48}$ bias.

268

269
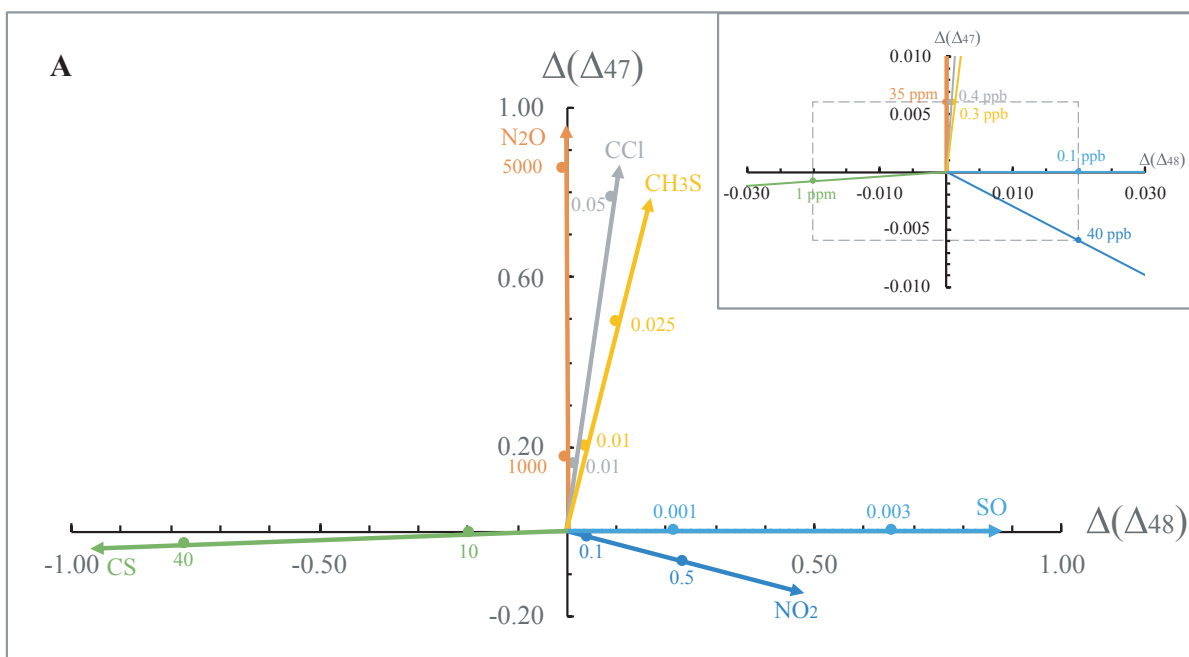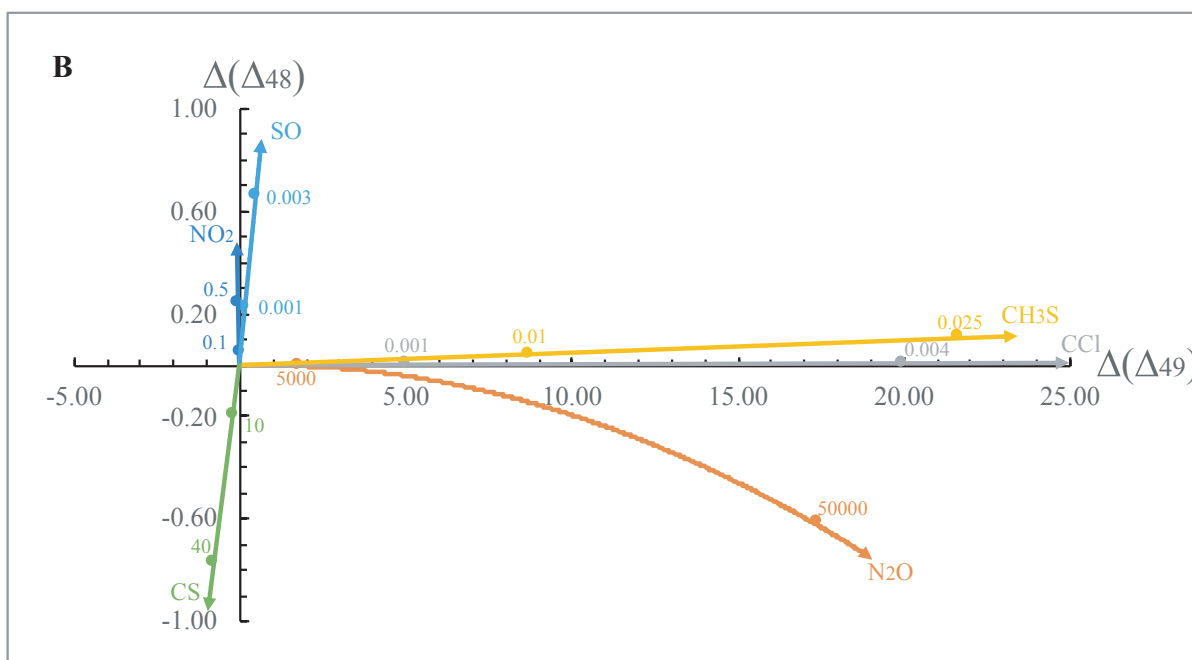
Fig. 2. Biases ($\Delta(\Delta_i)$) in the carbonate clumped isotope composition introduced by the presence of trace amounts of NO_2, N_2O, CH_3S, CS, CCl and SO in analyte CO_2. A: Δ_{47} vs. Δ_{48}; B: Δ_{48} vs. Δ_{49}. Arrows represent contamination vectors with H, C, N, O, S and Cl isotope compositions of interfering molecules corresponding to VSMOW, VPDB-CO_2, V-Air-N_2, VPDB-CO_2, VCDT and SMOC, respectively, and analyte CO_2 isotope compositions corresponding to VPDB-CO_2 and stochastic distribution of isotopes. Numbers in A and B provide contribution of interferent to CO_2 pool in ppm. Inset in A presents a zoom-up of A showing isobaric biases on a scale corresponding to the 2 SE of Δ_{47} and Δ_{48} measurements of ±6 ppm and ±20 ppm, respectively, that are typically obtained for 8 replicate measurements. For further discussion see Section 3.1.

Relative to NO_2, Δ_{47} and Δ_{48} values are less sensitive to contamination by N_2O, with Δ_{47} being much more affected than Δ_{48}. The bias in Δ_{47} becomes comparable to the upper limit of our analytical Δ_{47} precision of +6 ppm if the molar fraction of N_2O reaches 35 ppm. If this fraction increases to 5000 ppm, the bias in Δ_{47} reaches 856 ppm, while the corresponding Δ_{48} bias (-3 ppm) still remains well below its detection limit. Within this range, N_2O contamination would be indicated by a near-vertical displacement of measured Δ_{47} and Δ_{48}, relative to unbiased values. A significant bias in Δ_{48} is only introduced if the $\delta^{18}O$ of N_2O contaminant differs from that of the analyte CO_2. For example, if the contaminant $\delta^{18}O$ deviates by ∓50‰ from the analyte CO_2, biases of ±50 ppm in Δ_{48} are obtained for an addition of 1000 ppm N_2O, finally reducing the slope of the N_2O contaminant vector from near-infinity to values of 3.6 and -3.3, respectively. Contamination with CCl fragment also affects Δ_{47} much more than Δ_{48}. Over the range of natural variations in $\delta^{13}C$ and $\delta^{37}Cl$ values, contamination by CCl is indicated by a slope of ~8 in Δ_{47} vs Δ_{48} space, with both Δ_{47} vs Δ_{48} being positively biased. A similarly steep slope of ~4.6, on the contrary, would be indicative of CH_3S contamination. Presence of SO would be indicated by a horizontal vector in dual clumped isotope space, since mass 48 represents the lightest SO isotopologue. SO contamination would become detectable in Δ_{48} if its molar fraction in the CO_2 analyte pool makes up ≥ 0.1 ppb. For example, the presence of 0.1 ppb SO would introduce a bias of 20 ppm in Δ_{48}, and this bias scales linearly with the molar fraction of SO. Though CS does not have m/z 48 isotopologues, it affects Δ_{48} through the stochastic composition much more than Δ_{47}, resulting in a slightly positive slope of ~0.04. Of all contaminants investigated in this study, it is the only one that introduces negative biases both in Δ_{47} and Δ_{48} values.

Correlations between Δ_{48} and Δ_{49} could also be used to obtain further constraints on the nature and presence of contaminants (Fig. 2b). This should work most effectively for CCl, which introduces a bias in Δ_{49} that is ca. 2500 and 300 times larger than that in Δ_{48} and Δ_{47}, respectively, largely independent of the isotopic composition of the contaminant gas and analyte CO_2. Biases due to CH_3S occur magnified in Δ_{49} by factors of ~200 and ~40 relative to the

corresponding biases in Δ_{48} and Δ_{47}, respectively. For CS and SO, the bias in Δ_{49} represents roughly 100 % (slope ~1) and 75 % (slope ~1.35) of the bias observed in Δ_{48}, again largely independent of natural variations in the abundances of C, S and O isotopes. NO_2 bias in Δ_{49} is inversely correlated with the (positive) bias in Δ_{48}. Over the natural range of isotope variations in NO_2 and CO_2, its absolute value, however, only makes up 10-50 % of the Δ_{48} bias. Considering that the 2 SE of Δ_{49} measurements based on 8 replicate measurements can reach ±1000 ppm under most stable analytical conditions (Bernecker et al., 2023), isobaric contamination of CO_2 with NO_2 and SO becomes detectable by means of Δ_{49} at relatively high levels of contamination only, i.e., when the bias in Δ_{48} becomes > 1 ‰ (Fig. 2b) such that Δ_{48} values well outside the natural range would be obtained. Although N_2O has no m/z 49 isotopologues, Δ_{49} becomes sensitive to N_2O contamination via its effects on the stochastic composition at relatively high concentrations of several thousands of ppm.

3.2 Dual clumped isotope analysis

Final sample data pooling over all sessions is provided in Table 1, together with fully propagated errors (2 SE), which also take into account uncertainties associated with data normalization. PBL corrected δ^{45}-δ^{49} data of all replicates (input data for D47crunch) is listed in Supplementary Table S2.

The last session in which ETH-3 bleaching tests were performed was also evaluated individually in two more modes (see Sections 2.3, 4.3 and 4.8). Corresponding sample data is listed in Supplementary Tables S3 and S4.

Sample	N	$\delta^{13}C_{VPDB}$	1 SD	$\delta^{18}O_{VSMOW}$	1 SD	$\Delta_{47, CDES90}$	2 SE	$\Delta_{48, CDES90}$	2 SE
reference carbonates									
GU1	149	-7.73	0.03	12.83	0.12	0.225	0.002	-0.400	0.008
ETH-1	595	2.02	0.06	37.02	0.06	0.207	0.001	0.128	0.003
ETH-2	585	-10.17	0.04	19.88	0.10	0.209	0.001	0.130	0.003
ETH-1$_{QZ}$	2	2.07	0.01	37.11	0.03	0.200	0.013	0.118	0.042
ETH-2$_{QZ}$	1	-10.19		19.73		0.199	0.018	0.170	0.058
ETH-3$_{OXI}$	34	1.69	0.02	37.42	0.05	0.614	0.004	0.248	0.014
Carrara	126	1.97	0.06	37.66	0.10	0.309	0.002	0.146	0.006
Car-Py	9	1.93	0.04	37.69	0.04	0.309	0.006	0.143	0.021
experimental									
BW-33.7	8	-4.09	0.02	26.72	0.07	0.551	0.006	0.313	0.022
BW-33.7$_{QZ}$	7	-4.09	0.01	26.64	0.03	0.554	0.007	0.278	0.023
BW-33.7$_{OXI, QZ}$	5	-4.11	0.01	26.59	0.02	0.570	0.008	0.237	0.027
pedogenic									
HGB-42a	5	-3.65	0.03	29.41	0.07	0.575	0.008	0.363	0.029

Sample	n	δ13C		δ18O					
HGB-42a$_{QZ}$	1	-3.53		29.45		0.573	0.017	0.392	0.058
HGB-42a$_{NEW, QZ}$	2	-3.81	0.01	29.46	0.01	0.575	0.013	0.386	0.042
HGB-42a$_{NEWEST, QZ}$	6	-2.77	0.01	29.49	0.03	0.563	0.008	0.444	0.028
HGB-42a$_{NEWEST, OXI, QZ}$	7	-2.83	0.01	29.59	0.06	0.611	0.007	0.259	0.023
HGB-42a$_{NEWEST, OXI2}$	7	-2.80	0.01	29.47	0.04	0.606	0.007	0.256	0.023
HGB-42a$_{NEWEST, RINSE}$	5	-2.82	0.02	29.51	0.04	0.599	0.008	0.309	0.028
authigenic									
Carb2A	10	-42.98	0.16	43.11	0.04	0.661	0.006	0.273	0.020
Carb2A_bleach	8	-42.90	0.20	43.05	0.04	0.661	0.007	0.288	0.022
Carb3C	6	-50.87	0.13	43.93	0.05	0.614	0.008	0.289	0.025
Carb3C_bleach	6	-50.66	0.06	43.87	0.04	0.610	0.008	0.320	0.026
warm-water corals									
A4	5	-0.55	0.04	35.70	0.04	0.623	0.008	0.173	0.025
A4-V	5	-0.56	0.03	35.70	0.03	0.617	0.008	0.192	0.025
A6	5	0.16	0.02	36.43	0.04	0.613	0.008	0.185	0.025
A6-V	5	0.10	0.03	36.42	0.05	0.612	0.008	0.199	0.025
cold-water corals									
LP-SM-G	8	-4.94	0.08	40.13	0.19	0.711	0.007	0.192	0.021
LP-SM-U	7	-5.75	0.12	39.77	0.10	0.713	0.007	0.177	0.022
Brachiopods									
Mv130b_c	8	-2.78	0.07	37.93	0.06	0.689	0.007	0.247	0.022
Mv130b_uc	9	-1.71	0.05	38.14	0.05	0.683	0.006	0.236	0.021
MbHb_c	9	0.90	0.05	38.87	0.05	0.687	0.006	0.287	0.021
MbHb_uc	10	2.15	0.07	39.11	0.05	0.682	0.006	0.281	0.020
Echinoid spicules									
SD-MAI-S	7	-1.21	0.01	39.57	0.04	0.667	0.007	0.258	0.022
SD-MAI-S2	6	-1.37	0.02	39.55	0.05	0.630	0.007	0.433	0.025
SD-MAI-S2$_{QZ}$	2	-1.35	0.01	39.62	0.02	0.625	0.013	0.369	0.043
eggshells									
KASU_NOT	13	-14.00	0.06	37.76	0.07	0.568	0.005	0.266	0.017
KASU_NOT_CLEAN	7	-14.02	0.06	37.33	0.05	0.570	0.007	0.256	0.022
KIWI_INC	12	-9.83	0.05	32.45	0.11	0.556	0.005	0.258	0.017
KIWI_INC_CLEAN	8	-9.84	0.02	32.32	0.03	0.560	0.007	0.254	0.020
bioapatite									
SLGDenA	1	-3.20		40.29		0.621	0.019	0.450	0.065

Table 1. Bulk and dual clumped isotope composition of CO_2 evolved from phosphoric acid digestion of investigated samples. $\delta^{13}C$, $\delta^{18}O$ and Δ_i values are reported in ‰-deviation relative to V-PDB, V-SMOW and stochastic clumping. Number of replicates is indicated by n. Suffixes "G", "V", "c", "CLEAN", "bleach" and "OXI" indicate samples pretreated with 3 wt-% NaOCl.

3.3 Raman Spectroscopy

Four characteristic Raman modes of calcite can be clearly identified in the Raman spectra of the transparent large single calcite crystal (I), BW-33.7 (II) and SD-MAI-S2 (III) at around

334 1086, 711, 281 and 156 cm^{-1} (Fig. 1). We also observed a weak peak at 1066 cm^{-1} close to the

335 symmetrical stretching mode of CO_3 groups at 1086 cm^{-1} in samples I and II.

336

337 **4 Discussion**

338 **4.1 Isobaric contamination from NO_2**

339 <u>Experimentally precipitated calcite using $Ca(NO_3)_2$</u>

340 The synthetic calcite that was precipitated from an equilibrated DIC pool using $Ca(NO_3)_2$ (BW-

341 33.7) exhibits a significant $+\Delta_{48}/-\Delta_{47}$ disequilibrium offset with respect to its formation

342 temperature of 33.7°C, irrespective if it was reacted in a quartz (BW-33.7$_{QZ}$) or in a silver

343 capsule (BW-33.7) (Fig. 3a). The bleached aliquot reacted in a quartz capsule (BW-33.7$_{OXI, QZ}$)

344 plots indistinguishable from the dual clumped isotope composition predicted for that sample

345 according to the equilibrium $\Delta_{47} - \Delta_{48} - 1/T$ relationship of Fiebig et al. (2021). The observed

346 disequilibrium offset in the untreated samples describes a slope of -0.26 ± 0.18 that is consistent

347 with the slope of -0.30 characteristic of NO_2 contamination (Fig. 3a).

348

349 <u>Pedogenic carbonate HGB-42a</u>

350 The dual clumped isotope compositions of the different aliquots of sample HGB-42a are

351 displayed in Figure 3b. The two bleached pedogenic carbonate aliquots, reacted in silver (HGB-

352 42a$_{NEWEST, OXI2}$) and quartz capsule (HGB-42a$_{NEWEST, OXI, QZ}$), respectively, exhibit Δ_{47} and Δ_{48}

353 values that are indistinguishable from equilibrium. On the contrary, all non-bleached aliquots

354 from the same nodule, either reacted in quartz or silver capsules, depart significantly from

355 equilibrium, plotting below the equilibrium line. Of these, the aliquot exposed to water (HGB-

356 42a$_{NEWEST, RINSE}$) exclusively shows the smallest disequilibrium offset. Error-weighted linear

357 regression over all aliquots yields a slope of -0.26 ± 0.06 which – within its uncertainty –

358 corresponds to the slope theoretically predicted for NO_2 contamination of -0.30 (Fig. 3b).

359

360 <u>Spicule SD-MAI-S</u>

361 The untreated spicule reacted in a silver capsule (SD-MAI-S) plots slightly above the Δ_{47}/Δ_{48}

362 equilibrium line (Fig. 3c). Its Δ_{47} value indicates a precipitation temperature that is significantly

363 lower than the true temperature of formation of 8.5°C. Accordingly, the dual clumped isotope

364 composition of this sample may have been affected by CO_2 absorption kinetics. The plasma-

365 ashed aliquots reacted in a silver (SD-MAI-S2) and in a quartz capsule (SD-MAI-S2$_{QZ}$), on the

366 contrary, plot significantly below the equilibrium line, and the corresponding Δ_{47} values now

367 indicate a formation temperature that is significantly higher than 8.5°C. Again, the observed

differences in the dual clumped isotope compositions between these three samples would be in agreement with SD-MAI-S2 being affected by NO_2 contamination (Fig. 3c).
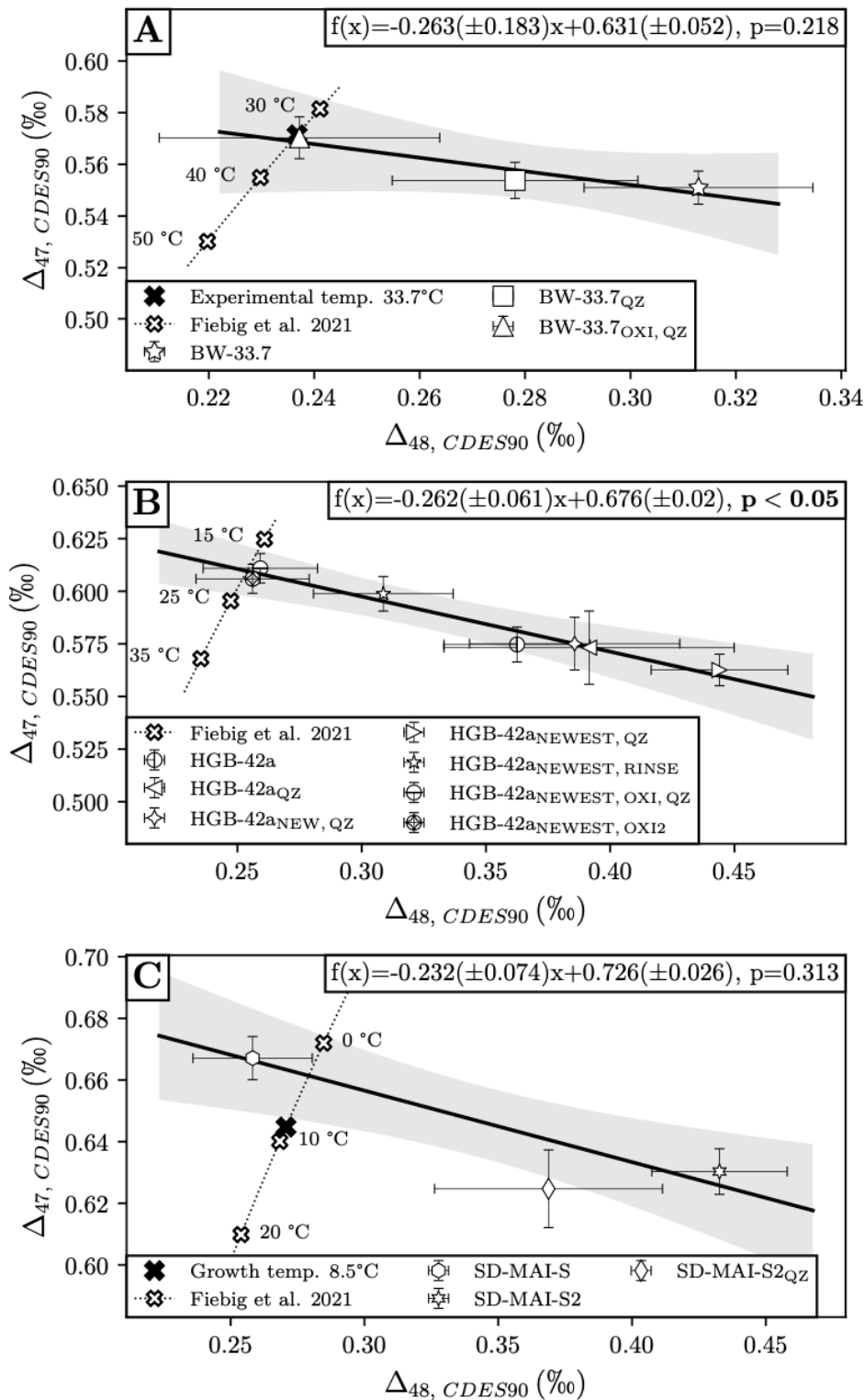

Fig. 3. Dual clumped isotope composition of unbleached and bleached aliquots of BW-33.7 (A) and HGB-42a (B), and of untreated (SD-MAI-S) and plasma-ashed (SD-MAI-S2) spicule (C). Error bars display fully propagated 2 SE (95 % confidence interval level). Solid line represents OGLS regression through sample-specific data points (Daëron & Vermeesch, 2024).

ETH-3 and other internal and external carbonate reference materials

Although we exclusively use CO_2 equilibrated at 1000°C and 25°C, respectively, for the projection of mass spectrometric raw data to the CDES 90, we have regularly run ETH-1, ETH-2 and ETH-3 (reacted in silver capsules) along with unknown carbonate samples. Recently, we documented that our long-term average Δ_{47} values for ETH-1 and ETH-2 confirmed the internationally agreed upon Δ_{47} values of 0.2052 ± 0.0016 ‰ (n = 232) and 0.2085 ± 0.0015 ‰ (n = 215), respectively, within their corresponding 1 SE uncertainties. Our long-term Δ_{47} value for ETH-3, however, occurred 10 ppm lower than its assigned value of 0.6132 ± 0.0014 ‰ (Bernecker et al., 2023). Interestingly, session mean values for ETH-3 show a significant (p-value < 0.005) correlation between Δ_{47} and Δ_{48} values (Fig. 4d). The error-weighted linear regression slope of -0.31 ± 0.15 agrees very well with that characteristic of NO_2 contamination. On the contrary, any significant correlations between session's mean Δ_{47} and Δ_{48} values are not displayed for Carrara, ETH-1, ETH-2 and GU1 (Fig. 4a-c, e).
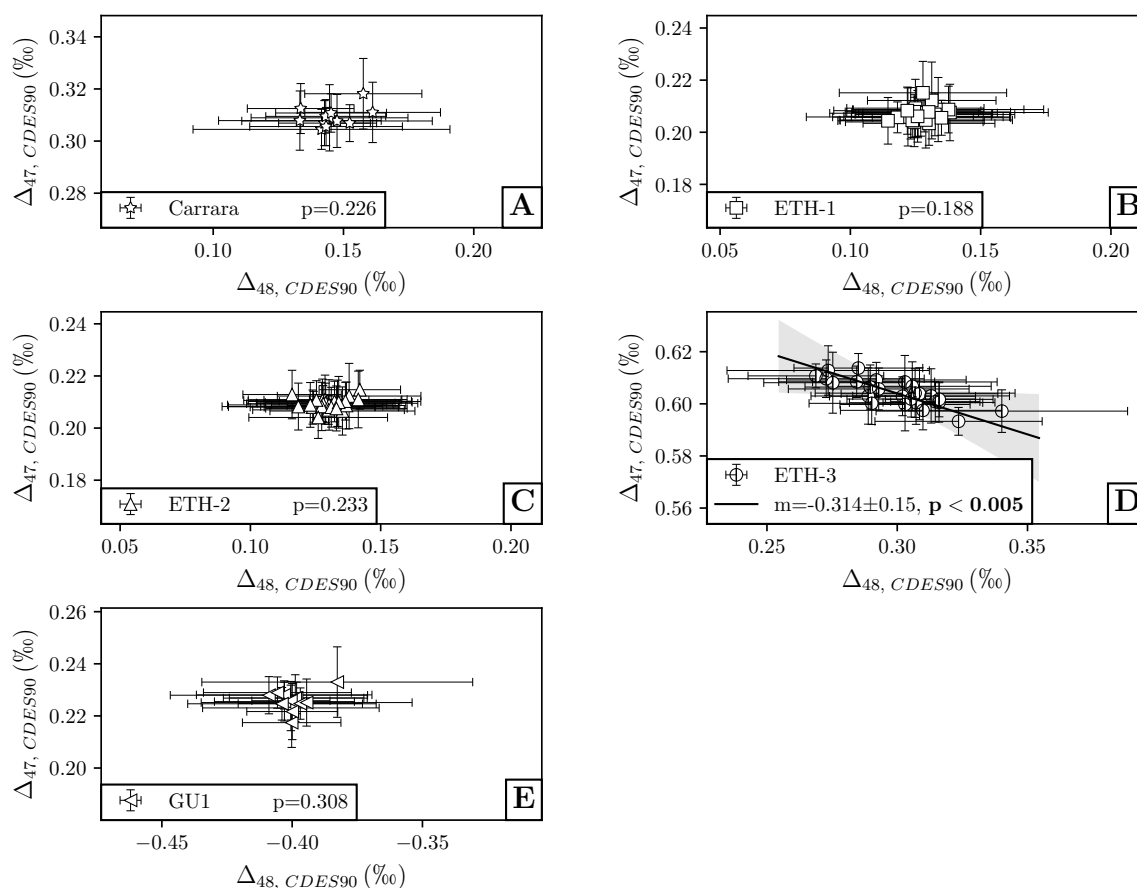
Fig. 4. Session-mean Δ_{47} and Δ_{48} values of unbleached aliquots of Carrara marble (A), ETH-1 (B), ETH-2 (C), ETH-3 (D) and GU1 (E). Error bars display 2 SE (95 % confidence interval level) based on long-term repeatability. Pearson tests reveal that only ETH-3 (D) displays a significant correlation (p < 0.05) between Δ_{47} and Δ_{48} values. Solid line (D) represents OGLS regression through all data points (Daëron & Vermeesch, 2024).

4.2 Origin of NO_2 interferent

395   The extent of NO_2 bias in Δ_{47} and Δ_{48} values of non-bleached aliquots of BW-33.7 (Fig. 3a),

396   HGB-42a (Fig. 3b), SD-MAI-S2 (Fig. 3c) and ETH-3 (Fig. 4d) likely does not depend much

397   on the choice of capsule material. Non-bleached BW-33.7 reacted in quartz capsules has Δ_{47}

398   and Δ_{48} indistinguishable from those of the same sample reacted in silver capsules (Table 1,

399   Fig. 3a). The spicule aliquot reacted in a quartz capsule (SD-MAI-S2$_{QZ}$) has a significantly

400   lower Δ_{48} value than the aliquot reacted in silver (SD-MAI-S2), but was analyzed in two

401   replicates only (Table 1, Fig. 3c).

402   BW-33.7 was precipitated using a $Ca(NO_3)_2$ solution. Traces of nitrate might, therefore, still be

403   present within this sample. It has been well demonstrated by Hu et al. (2019) that nitrate

404   decomposes to NO_2 in the presence of phosphoric acid and in the absence of any silver. These

405   authors reacted 2 mg of calcite doped with 1 mg of KNO_3 at 72°C in a McCrea reaction vessel

406   with 100% H_3PO_4. They acquired Raman spectra on the produced gas and noticed a mode at

407   752 cm^{-1} that is characteristic of NO_2. They also extracted CO_2 from mixtures of 100-200 μg

408   of $CaCO_3$ and ~50μg of KNO_3 using the Gas Bench II setup, where the mixture was reacted

409   with 6-8 drops of phosphoric acid at 72°C for 4 h in borosilicate Exetainer topped with butyl

410   rubber septum. Although the CO_2 was passed in a He carrier gas over a PoraPlot Q column (25

411   m, 0.32 mm o.d.) at 70°C before being introduced into the gas source mass spectrometer, they

412   noticed an abnormal increase of the m/z 46 background, indicating the presence of $^{14}N^{16}O^{16}O$

413   in the eluted CO_2 (Hu et al., 2019). These authors proposed the following reactions to be

414   responsible for NO_2 production from nitrate:

415    $NO_3^- + H^+ \rightarrow HNO_3$ (1)

416    $4\ HNO_3 \rightarrow 4\ NO_2 + O_2 + 2\ H_2O$ (2)

417   We have investigated BW-33.7 and SD-MAI-S2 using Raman spectroscopy. Up to now, no

418   study has been reported about a possible substitution of NO_3 groups with CO_3 groups in calcite,

419   which was detected by Raman spectroscopy. In the case of a possible incorporation of NO_3

420   groups in calcite, we are expecting a shift, broadening of Raman modes, or the presence of a

421   characteristic mode of NO_3 groups as a weak peak. According to the literature, the characteristic

422   mode of NO_3 is located in the range of 1040-1069 cm^{-1} in different nitrates (Liu et al., 2008;

423   Hetmańczyk et al., 2009; Bishop et al., 2021). Most of them are in the range of 1043-1056 cm^{-1},

424   especially in calcium nitrates. Liu et. al. (2008) used Raman spectrometry to study the

425   hygroscopic behavior of individual $Ca(NO_3)_2$ and internally mixed $Ca(NO_3)_2/CaCO_3$ particles.

426   They identified NO_3 groups based on the symmetrical stretching mode v_1. An isolated free NO_3

427   ion has this characteristic mode at 1049 cm^{-1}, which shifts from 1050 cm^{-1} to 1056 cm^{-1} with

428   decreasing humidity in the presence of Ca^{2+} in $Ca(NO_3)_2$. We also observed a weak peak at

429   1066 cm^{-1} close to the symmetrical stretching mode of CO_3 groups at 1086 cm^{-1} in samples I

430   and II. Our measurements reveal a detection limit of 0.7 - 0.5 % for this peak in these two

431   samples. For sample SD-MAI-S2 (III) the detection limit was > 1 %, probably explaining why

432   this peak is not detected in this sample. Though we cannot entirely exclude it, we do not think

433   this peak is indicative of nitrate, either present in calcite as $Ca(NO_3)_2$ or substituted for CO_3^{2-}.

434   First, this peak is well outside the range of 1043 cm^{-1} to 1056 cm^{-1} that is typical for $Ca(NO_3)_2$,

435   which has been used to prepare sample BW 33.7. Second, we do not detect any shift and

436   broadening of all Raman modes of calcite structure which would be expected if nitrate

437   substitutes for carbonate. Instead, we propose its occurrence is best explained by the presence

438   of small amounts of ikaite ($CaCO_3*6H_2O$) (Sánchez-Pastor et al., 2016) which may have

439   formed on the surface of the calcite through the absorption of moisture. Note that the presence

440   of only 350 ppb of NO_2 in the analyte CO_2 pool is required to explain the observed bias in Δ_{47}

441   and Δ_{48} in BW-33.7 relative to the expected equilibrium composition. This is well below the

442   detection limit of nitrate of 1000 ppm characteristic of spontaneous Raman spectroscopy (Diaz

443   & Hahn, 2020; Schlack et al., 2021).

444   Spicule samples SD-MAI-S is composed of magnesium calcite. Spicules usually contain 0.1 %

445   (w/w) organic matrix which is mainly composed of proteins and glycoproteins (e.g., Ameye et

446   al., 1999). Proteins, in general, can contain up to 20 % of reduced nitrogen (Krul et al., 2019).

447   Apparently, reduced nitrogen in the organic matrix is oxidized to nitrate when the powdered

448   spicule is treated with molecular oxygen in the plasma asher. As for BW-33.7, the presence of

449   only 350 ppb of NO_2 in the reacted CO_2 is required to explain the isotopic bias observed in SD-

450   MAI-S2 relative to the untreated SD-MAI-S (Fig. 3c). Considering SD-MAI-S to be unbiased,

451   as suggested by its position above the equilibrium line characteristic of CO_2 absorption, we

452   postulate that reduced nitrogen in organic matter needs not be removed from carbonate for

453   accurate dual clumped isotope analysis.

454   Trace amounts of nitrate, as indicated by NO_2 bias in Δ_{47} and Δ_{48} values of non-bleached

455   aliquots, even seem to be present in pedogenic carbonate sample HGB-42a and ETH-3. ETH-

456   3 is composed of Cretaceous chalk which consists of carbonate skeletons of marine

457   phytoplankton and micritic carbonate. It has a non-carbonate content of less than 2 %

458   (Neumann, 2012). Phytoplankton cells utilize seawater nitrate as their nitrogen source (e.g.,

459   Kim et al., 2022). Traces of nitrate, therefore, might still be contained in the organic remnants

460   within ETH-3.

461

462   **4.3 Removing nitrate contaminant from carbonates**

All bleached aliquots of BW-33.7 and HGB-42a have in common that they exhibit significantly higher Δ_{47} and lower Δ_{48} values than their unbleached counterparts, demonstrating that nitrate contamination and NO_2 interference is significantly suppressed in bleached aliquots (Figs. 3a, b). Overnight treatment of samples with distilled water also reduces isobaric bias in Δ_{47} and Δ_{48}, however, this alone is not sufficient to quantitatively remove the NO_2 interference, as demonstrated by the observation that HGB-42a$_{NEWEST, RINSE}$ still plots significantly below the equilibrium line, whereas the two bleached aliquots of the same sample (HGB-42$_{NEWEST, OXI2}$ and HGB-42a$_{NEWEST, OXI, QZ}$) plot indistinguishable from the equilibrium line (Fig. 3b). We postulate that the nitrate contaminant in this sample is contained in organic matter and is most effectively dissolved after quantitative oxidation of organic matter to CO_2.

In order to test in more detail to what extent ETH-3 is affected by nitrate contamination and if the contaminant can be effectively removed through pre-treatment with 3 wt-% NaOCl we performed a sequential bleaching test and analyzed unbleached, once- and twice bleached aliquots of ETH-3 within the same session. In this session, the repeatability of Δ_{49} measurements was excellent (1100 ppm) so that we also projected Δ_{49} data to the CDES 90. Once (ETH-3$_{OXI}$, ETH-3$_{NEW, OXI}$) and twice bleached (ETH-3$_{OXI2}$) aliquots of ETH-3 all have indistinguishable Δ_{47} and Δ_{48} values and center around the equilibrium line (Fig. 5a). On the contrary, the two unbleached aliquots came out with lower Δ_{47} and higher Δ_{48} values than their bleached counterparts. As already observed for session mean values of unbleached ETH-3 aliquots (Fig. 4d), the slope of -0.23 ± 0.11 for the error-weighted linear regression line through all data points is consistent again with NO_2 contamination (Fig. 5a). The correlation between Δ_{48} and Δ_{49} values independently supports the contention of NO_2 contamination in untreated ETH-3 (Fig. 5b). Whereas unbleached aliquots exhibit significantly higher Δ_{48} values than bleached aliquots, Δ_{49} values for bleached and unbleached aliquots of ETH-3 are within errors indistinguishable from each other – as is predicted for sub-ppm levels of NO_2 contamination (Fig. 2b; Fig. 5b).
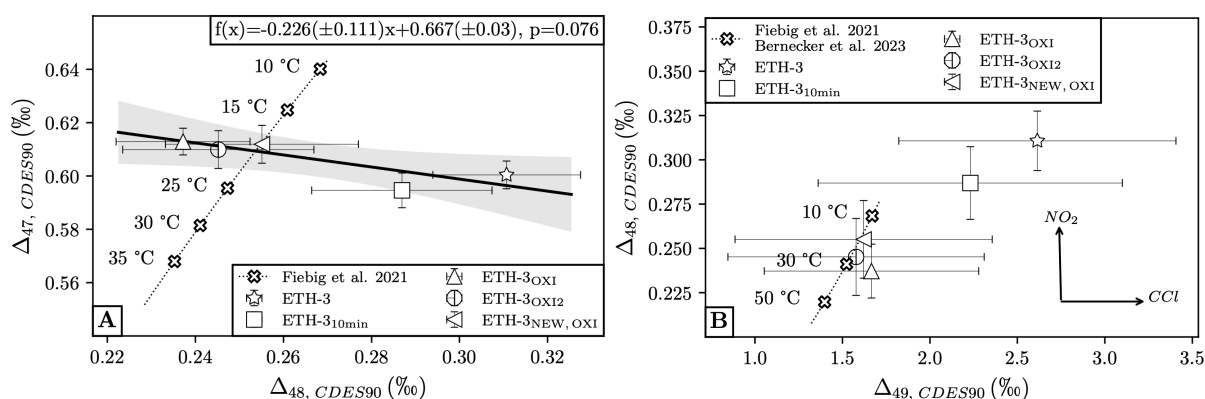
Fig. 5. Dual clumped isotope composition of unbleached and bleached aliquots of ETH-3, analyzed alternatingly within a single session. Error bars display fully propagated 2 SE (95 % confidence interval level). (A) Δ_{47} vs Δ_{48}. Solid line represents OGLS regression through all data points (Daëron & Vermeesch, 2024); dotted line represents position of calcite equilibrium according to Fiebig et al. (2021). (B) Δ_{48} vs Δ_{49}. Dotted line represents position of calcite equilibrium according to Fiebig et al. (2021) for Δ_{48} and Bernecker et al. (2023) for Δ_{49}.

Three observations imply that a single bleaching step with 3 wt-% NaOCl is sufficient to effectively remove nitrate contaminant:

i) The once-bleached aliquot of BW-33.7 (BW-33.7$_{OXI, QZ}$) plots indistinguishable from the equilibrium line, and its Δ_{47} value corresponds within errors to its formation temperature of 33.7°C (Fig. 3a).

ii) Once (ETH-3$_{OXI}$, ETH-3$_{NEW, OXI}$) and twice-bleached ETH-3 (ETH-3$_{OXI2}$), all reacted in silver capsules, yield indistinguishable Δ_{47} and Δ_{48} values, centering around the equilibrium line at a temperature of 18°C (Fig. 5a).

iii) A sequential bleaching test was also performed on pedogenic carbonate sample HGB-42a. HGB-42a$_{NEWEST, OXI2}$, which was bleached twice, has Δ_{47} and Δ_{48} values identical to HGB-42a-$_{NEWEST, OXI, QZ}$, which was just oxidized once (Fig. 3b).

Our results demonstrate that systematic bleaching tests should be performed on unknown samples in order to exclude potential bias through isobaric contamination. Tagliavento et al. (2023a) showed that bleached aliquots of bird eggshells (Kiwi, Cassowary) reproduced Δ_{47} and Δ_{48} values of unbleached aliquots, demonstrating that the excess Δ_{48} characteristic of all bird eggshells does not arise from isobaric interferences. Staudigel et al. (2024) bleached two of their authigenic methane seep carbonates, both of which covered the entire range of observed Δ_{47} and Δ_{48} values. Again, bleached aliquots confirmed Δ_{47} and Δ_{48} values of unbleached aliquots within errors, providing independent evidence that the observed trend in dual clumped isotope data in authigenic carbonates is real. For the study of Davies et al. (2022) on corals, bleached aliquots were run along with their unbleached counterparts for two warm-water coral samples (A4, A6). Since no significant differences were obtained between bleached and non-bleached aliquots, average Δ_{47} and Δ_{48} values were pooled over all replicates in that study, without making bleached and unbleached aliquots discernable.

A comprehensive comparison of dual clumped isotope data between bleached and non-bleached aliquots from a diverse range of natural carbonates is provided in Figure 6. In addition to the data discussed above, we further considered cold-water coral LP-SM for this comparison. Of all cold-water corals analyzed by Davies et al. (2022), LP-SM showed the largest departures in

19

$\varDelta_{47}$ and $\varDelta_{48}$ from expected equilibrium values. We also prepared new homogenized sample powder from Brachiopod specimen MV130b and MBHB, originally analyzed by Davies et al. (2023). These two specimens were selected as they cover the entire disequilibrium $\varDelta_{47}$ and $\varDelta_{48}$ range observed by Davies et al. (2023). In all cases, $\varDelta_{47}$ and $\varDelta_{48}$ values of bleached aliquots reproduce those obtained on non-bleached aliquots (Fig. 6). These results strongly imply that the carbonates analyzed in the studies of Davies et al. (2022, 2023), Tagliavento et al. (2023a) and Staudigel et al. (2024) were not suffering from nitrate contamination.
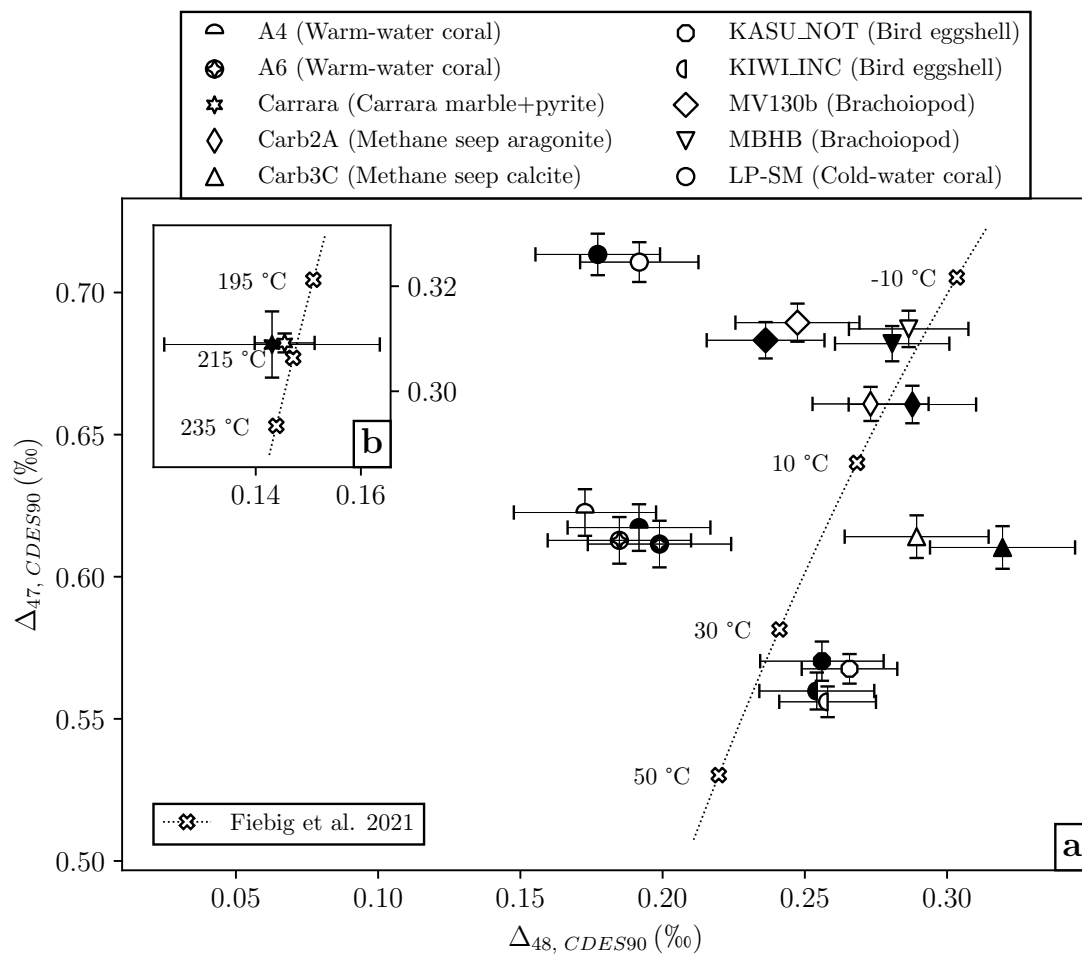
Fig. 6. (a) Comparison of dual clumped isotope compositions of unbleached (open symbols) and bleached (closed symbols) aliquots of carbonate powder acquired from Brachiopod shells, warm- and cold-water coral skeletons, eggshells and authigenic methane seep carbonates. Inset (b) shows the long-term $\varDelta_{47}$ and $\varDelta_{48}$ mean values of Carrara marble and Carrara marble doped with pyrite. Error bars display fully propagated 2 SE (95 % confidence interval level). Dotted line represents the position of calcite equilibrium (Fiebig et al., 2021).

4.5 Effects of NaOCl pre-treatment on the bulk isotope composition of carbonates

NO_2 isotopologues are isobaric to CO_2 on m/z 46-49. NO_2-related $\varDelta_{48}$ excesses of +200 ppm and +70 ppm, as are characteristic of HGB-42a and BW-33.7, respectively, should correspond

20

with biases in $\delta^{18}O$ of 0.1 ‰ and 0.04 ‰, respectively, whereas $\delta^{13}C$ should not be affected at all. This is largely consistent with measured bulk isotope compositions of unbleached and bleached aliquots of BW-33.7 and HGB-42a$_{NEWEST}$ (Table 1). $\delta^{13}C$ of unbleached (-4.09 ± 0.01 ‰, reacted in QZ, and -4.09 ± 0.02 ‰, reacted in silver) and bleached aliquots of BW-33.7 (-4.11 ± 0.01 ‰, reacted in QZ) are identical, whereas $\delta^{18}O$ of the bleached aliquot (26.59 ± 0.02 ‰) occurs slightly lower than the 26.64 ± 0.03 ‰ and 26.72 ± 0.07 ‰ obtained for unbleached aliquots reacted in quartz and silver, respectively. In case of HGB-42a$_{NEWEST}$, the $\delta^{13}C$ value of -2.77 ± 0.01 ‰ obtained for the unbleached aliquot (reacted in quartz) is hardly distinguishable from the -2.83 ± 0.01 ‰ (reacted in quartz) and the -2.80 ± 0.01 ‰ (reacted in silver) obtained for the once and twice-bleached aliquot, respectively. The observation that the $\delta^{13}C$ of the twice-bleached sample moves closer again to that of the unbleached one may imply that the parental powder from which these three aliquots were prepared might have not been perfectly homogenized. The same is suggested by $\delta^{18}O$ data. While a value of 29.49 ± 0.03 ‰ is obtained for the unbleached aliquot, the once and twice bleached aliquots yielded values of 29.59 ± 0.06 ‰ and 29.47 ± 0.04 ‰, respectively. Differences in $\delta^{13}C$ and $\delta^{18}O$ between unbleached, once- and twice-bleached aliquots of ETH-3 are within errors insignificant (Supplementary Table S3). While for most samples $\delta^{13}C$ and $\delta^{18}O$ values of treated and untreated aliquots agree well within external repeatabilities (1 SD), there are also some inconsistencies (Table 1): For the bleached Cassowary eggshell, $\delta^{18}O$ is 0.4 ‰ lower than for the unbleached aliquot, while $\delta^{13}C$ is reproduced within uncertainties. On the contrary, $\delta^{13}C$ values of both bleached aliquots of Brachiopod shells are shifted by -1 ‰ relative to unbleached aliquots, while $\delta^{18}O$ values between the two differ by only -0.2 ‰. Whenever prevalent, the observed shifts in bulk isotopic compositions are not unidirectional but seem to depend on the investigated archive. $\delta^{13}C$ and $\delta^{18}O$ values of bleached cold-water coral aragonite exceed those of the untreated aliquot by 0.8 ‰ and 0.4 ‰, respectively. Pre-treatment of warm-water coral aragonite, on the contrary, does not go along with any significant shifts in the bulk isotopic compositions (Table 1).

It has been investigated in several studies which is the best and most effective way to remove organic matter from carbonates prior to isotopic analysis. Gaffey & Bronnimann (1993) determined that 2.5 wt-% NaOCl is more effective than 30 wt-% H_2O_2. While recommendations in favor of H_2O_2 have been made (Keatings et al., 2006; Wierzbowski et al., 2007), a most recent comprehensive study demonstrated that H_2O_2 pretreatment can affect the bulk isotopic composition of carbonates ($\delta^{13}C$ plus $\delta^{18}O$) by up to 4 ‰, and may even affect Δ_{47} (Zhang et al., 2020). As summarized by the latter authors, several explanations have been offered for the

observed changes amongst which are the removal of organic matter, partial dissolution of carbonate, precipitation of $Ca(OH)_2$, isotopic exchange with the reagent, or the combination of all of these processes. Combined absolute changes in $\delta^{13}C$ and $\delta^{18}O$ accompanied with NaOCl pre-treatment applied in this study were < 1.5 ‰. However, even when significant changes in $\delta^{13}C$ and $\delta^{18}O$ were observed, Δ_{47} and Δ_{48} values of bleached aliquots reproduced those of unbleached aliquots within uncertainty (Table 1). We recommend interpreting $\delta^{13}C$ and $\delta^{18}O$ values of untreated aliquots for samples whose bulk isotopic compositions are significantly altered during NaOCl pre-treatment, i.e., whenever measured changes in $\delta^{13}C$ and $\delta^{18}O$ between treated and untreated aliquots exceed those predicted by our isobaric interference calculator for the observed concurrent changes in Δ_{47} and Δ_{48} values.

4.6 Isobaric contamination arising from SO

It has been postulated that reduced sulfur-bearing compounds may evoke isobaric interferences on m/z 48 and 49 through formation of SO (Guo & Eiler, 2007). Reduced sulfur compounds like pyrite are present as accessory minerals in authigenic carbonate deposits resulting from sulfate-driven anaerobic oxidation of methane. In order to investigate if the presence of pyrite in carbonates biases Δ_{48} under conditions specific for our analytical setup, internal Carrara carbonate standard was doped with 2 wt-% FeS, and this mixture subjected to phosphoric acid digestion at 90°C for 30 minutes (Staudigel et al., 2024). Δ_{47} and Δ_{48} values of the extracted CO_2 remained unchanged relative to the long-term averages obtained for Carrara-derived CO_2 (Table 1; Fig. 6b). This result demonstrates that the presence of pyrite as accessory mineral does not compromise carbonate Δ_{48} values, at least under the analytical conditions specific for HAL.

4.7 The effect of variance minimization of ETH-3 on Δ_{47} (CDES 90) and Δ_{48} (CDES 90) values presented in previous studies

The D47crunch module of Daëron (2021) that we use for data processing of PBL corrected δ^{45}-δ^{49} values, considers variance minimization of Δ_{47} and Δ_{48} values of anchors and unknown samples for the determination of session-specific correction parameters a, b and c. In our case, (unbleached) ETH-3 made up a significant fraction (8 % on average) of the total number of analyzed replicates per session. Since observed variances in Δ_{47} and Δ_{48} values of ETH-3 are affected by the extent of isobaric NO_2 contamination, it needs to be tested if and to what extent Δ_{47} (CDES 90) and Δ_{48} (CDES 90) values of unknowns reported in previous studies were biased by variance minimization of ETH-3. For this exercise, we have re-evaluated Δ_{47} and Δ_{48} values

of calcites closely reflecting isotopic equilibrium (Fiebig et al., 2021), aragonitic skeletons of cold- and warm-water corals (Davies et al., 2022), calcitic eggshells (Tagliavento et al., 2023a), calcitic Brachiopod shells (Davies et al., 2023) and authigenic methane seep carbonates (Staudigel et al., 2024) in this study, not considering ETH-3 for variance minimization. A comparison between previously published and reprocessed data demonstrates that variance minimization of ETH-3 has not significantly affected our previously published dual clumped isotope data such that the Δ_{47}-1/T and Δ_{48}-1/T equilibrium relationships of Fiebig et al. (2021) and all interpretations made in the aforementioned publications remain valid:
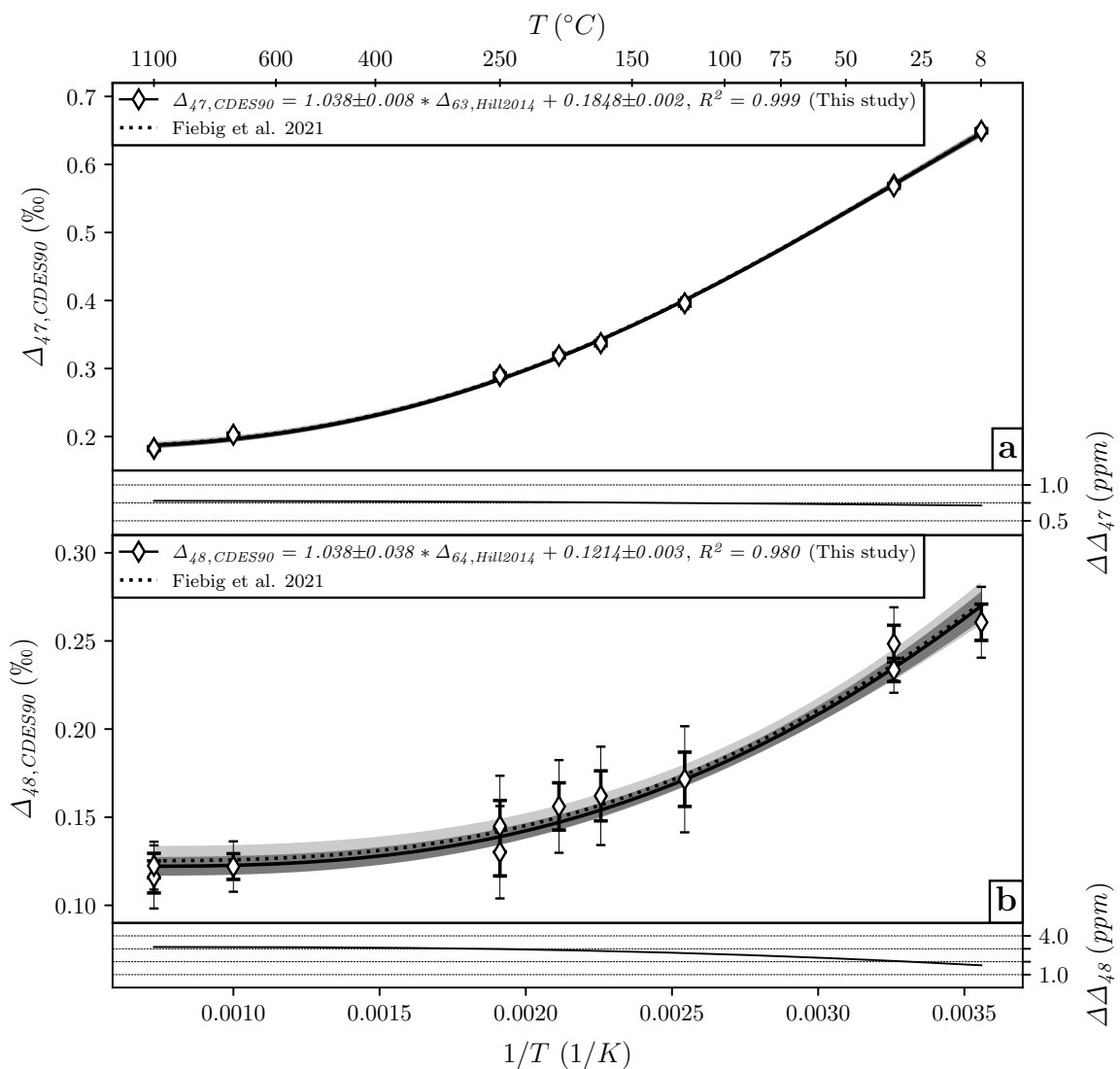
Fig. 7. Comparison of reprocessed Δ_{47}-1/T (a) and Δ_{48} -1/T (b) relationships with those originally determined by Fiebig et al. (2021). In order to express the temperature dependence of Δ_{47} and Δ_{48} values, fourth order polynomials perfectly describing the theoretical temperature dependence of Δ_{63} and Δ_{64} (Hill et al., 2014), respectively, were linearly adjusted to measured data by scaling factors and a constant term, considering error-weighted least squares regression (Fiebig et al., 2021). Relationships originally determined by Fiebig et al. (2021) are well within the 95 % and 68 % confidence intervals of reprocessed

relationships. Over the entire temperature range, the difference (Δ) between reprocessed and original calibrations is < 1 ppm for Δ_{47} and < 4 ppm for Δ_{48}.

1) Over a temperature range of 8° – 1100°C, the re-evaluated Δ_{47}-1/T and Δ_{48}-1/T equilibrium relationships are

Δ_{47} (CDES 90) (‰) = 1.038 (-5.897 1/T $-$ 3.521 10^3 1/T^2 + 2.391 10^7 1/T^3 $-$ 3.541 10^9 1/T^4) + 0.1848

Δ_{48} (CDES 90) (‰) = 1.038 (6.002 1/T $-$ 1.299 10^4 1/T^2 + 8.996 10^6 1/T^3 $-$ 7.423 10^8 1/T^4) + 0.1214

At any temperature, equilibrium Δ_{47} and Δ_{48} values predicted by these re-evaluated relationships differ by less than 1 ppm and 4 ppm, respectively, from the original equations provided by Fiebig et al. (2021). Re-processed calibrations are, therefore, well within the corresponding 95 % confidence intervals of the Δ_{47}-1/T and Δ_{48}-1/T regressions provided by Fiebig et al. (2021) (Figs. 7a, b)

2) Reprocessed disequilibrium Δ_{47} and Δ_{48} values for corals are compared to those published in Davies et al. (2022) in Figure 8. The reprocessed slope for the correction of cold-water coral data is -0.80 ± 0.04, and, hence, within its uncertainty still consistent with both the model-predicted and empirical slope of -0.78 of Davies et al. (2022).
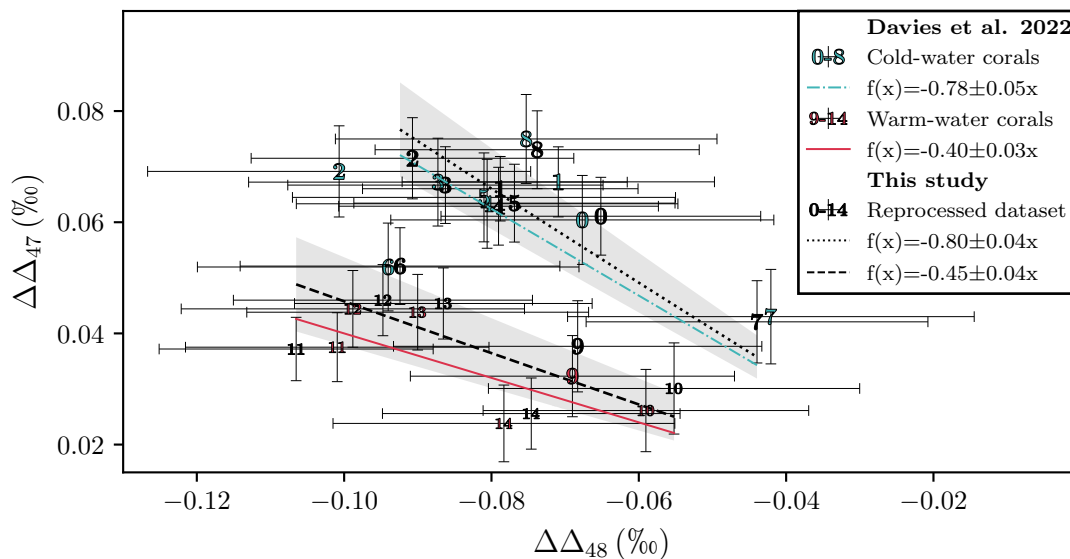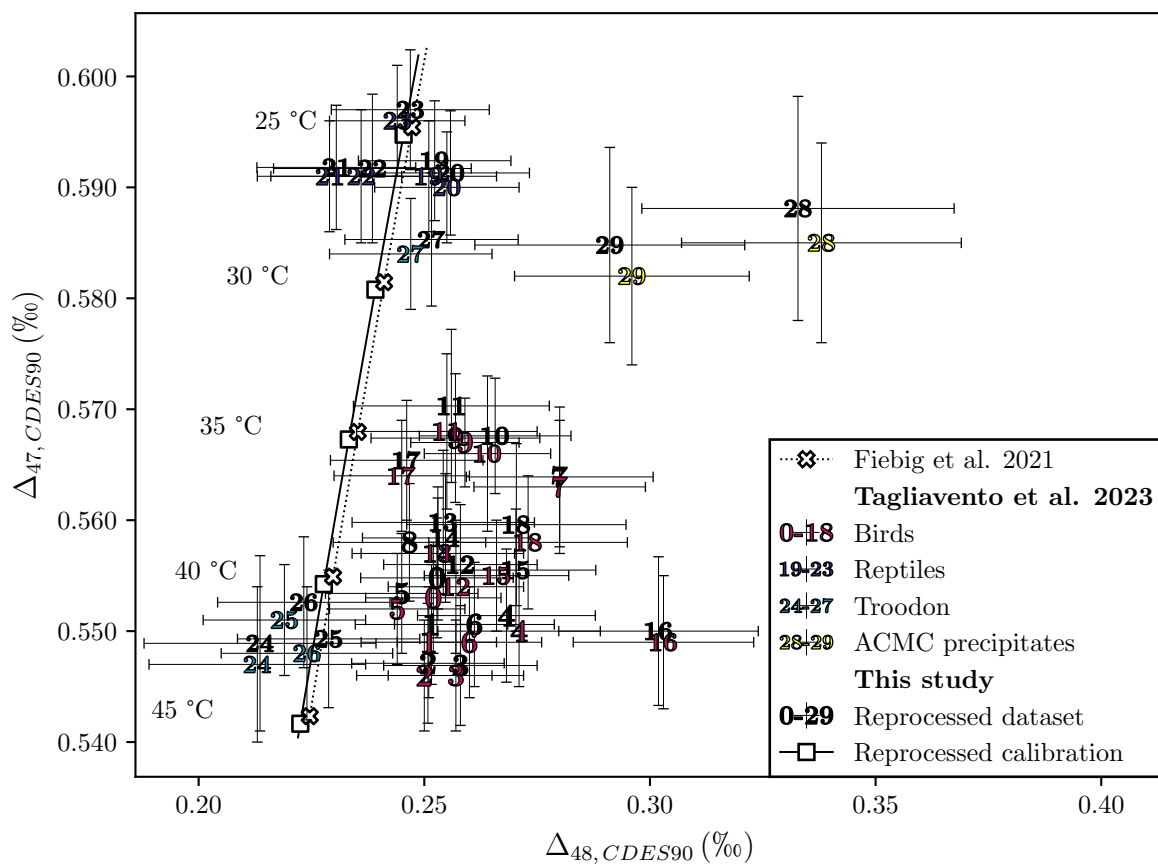

Fig. 8. Extent of disequilibrium (relative to Δ_i-values predicted by independently known growth temperatures and Δ_{47}-1/T and Δ_{48} -1/T equilibrium relationships of Fiebig et al. (2021)) recorded in the dual clumped isotope composition of carbonate skeletons from cold-and warm-water corals. Reprocessed and original disequilibrium offsets are indistinguishable from each other. For the cold-water corals, simple linear regression through reprocessed data and the origin yields a slope of -0.80 ± 0.04 that is – within errors – indistinguishable from both the empirical (-0.78 ± 0.05) and model-predicted slopes (-0.78) obtained by Davies et al. (2022). The reprocessed disequilibrium slope for the warm-water coral dataset is also indistinguishable from the original one (-0.45 ± 0.04 compared to -0.40 ± 0.03, Davies et al., 2022).

648

649   3) Troodon and reptile eggshell data still plots indistinguishable from the equilibrium line,

650   whereas the group of birds exhibits significant disequilibrium Δ_{48} offsets (Fig. 9).

651   4) The revised relationship between disequilibrium Δ_{47} and Δ_{48} in Brachiopod calcite is

652   indistinguishable from the one published by Davies et al. (2023), confirming that a diffusional

653   limitation is required in addition to unbalanced de(hydration)/(de)hydroxylation rates in order

654   to explain the data (Fig. 10).

655   5) The empirical slope by which authigenic methane seep carbonates depart from equilibrium

656   is indistinguishable from the one published by Staudigel et al. (2024) (Fig. 11). Within errors,

657   back-extrapolated temperature agrees well with measured vent temperature of 3.5°C.

658

Fig. 9. Dual clumped isotope composition of eggshells, relative to the position of calcite equilibrium. Comparison of reprocessed data with original data published by Tagliavento et al. (2023a). All reprocessed data is indistinguishable from originally published data.
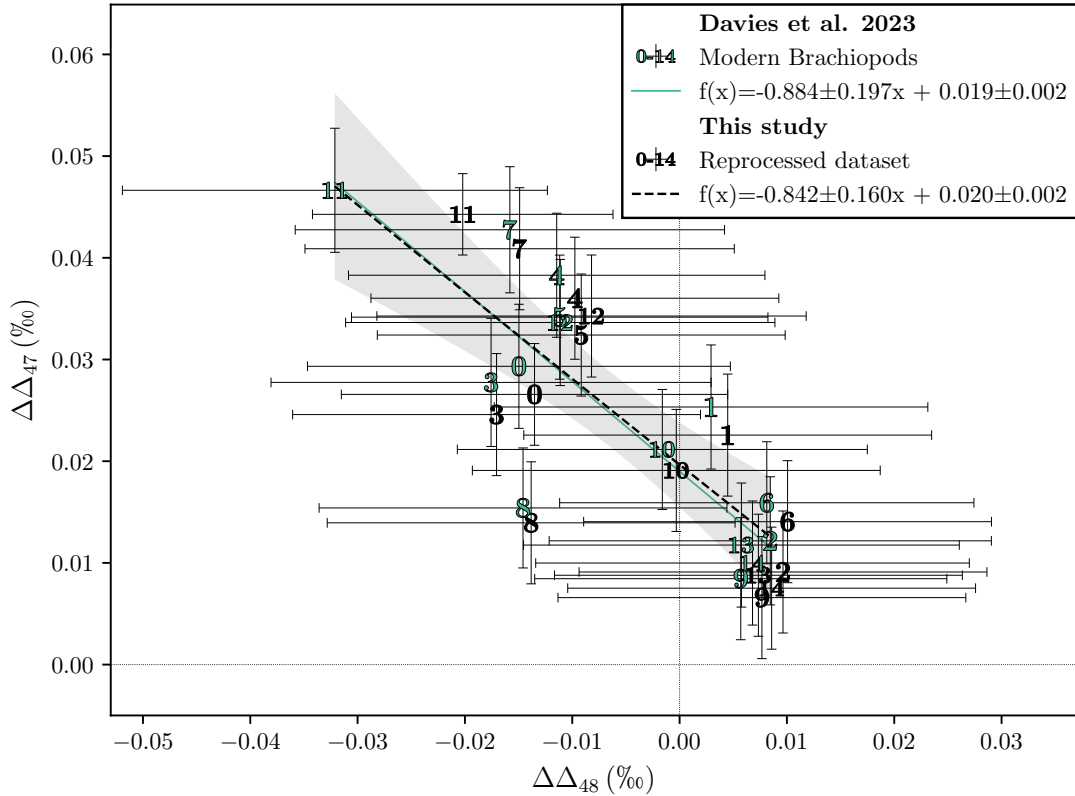
Fig. 10. Extent of disequilibrium (relative to Δ_I-values predicted by independently known growth temperatures and Δ_{47}-1/T and Δ_{48}-1/T equilibrium relationships of Fiebig et al. (2021)) recorded in the dual clumped isotope composition of Brachiopod shells. Reprocessed and original disequilibrium offsets are indistinguishable from each other, and so are the corresponding simple linear regressions.
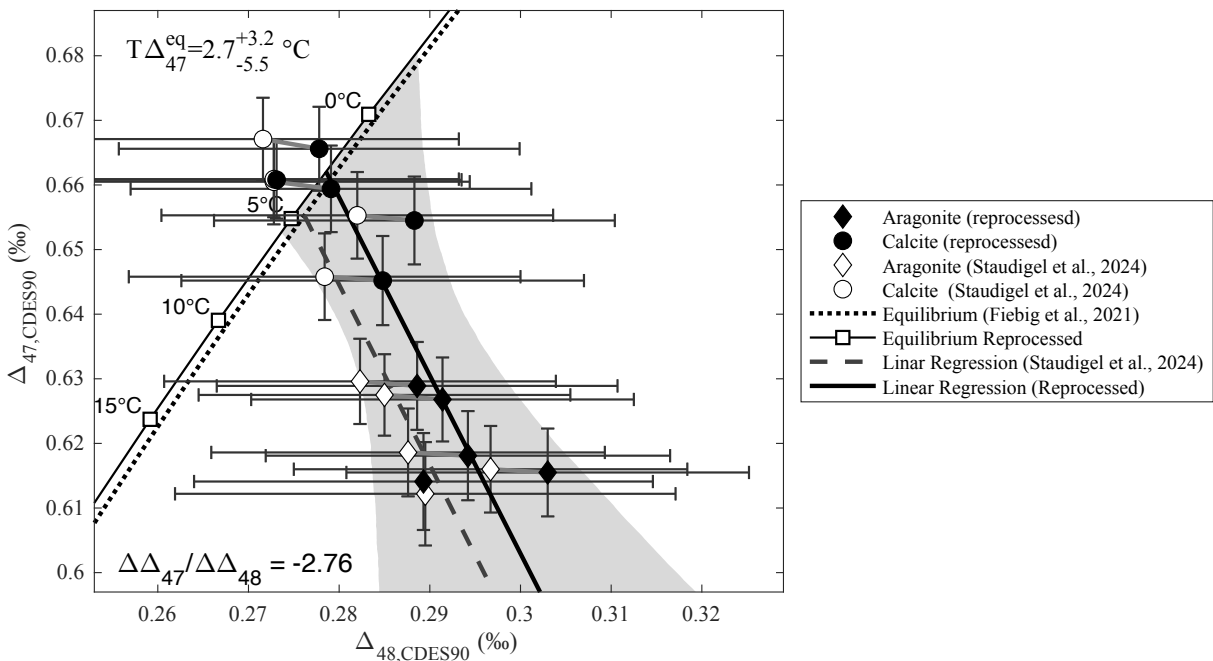
Fig. 11. Dual clumped isotope composition of authigenic methane seep carbonates, relative to the position of calcite equilibrium. Comparison of reprocessed data with original data published by Staudigel et al. (2024). Reprocessed dual clumped isotope data, slope of linear regression through reprocessed data and corresponding extrapolated vent temperature are indistinguishable from originally published data/values.

26

4.8 Implications for other analytical setups and the I-CDES

Fiebig et al. (2021) observed that I-CDES values (anchored relative to ETH-1, ETH-2 and ETH-3) for calcites precipitated closest to equilibrium were significantly higher than the corresponding CDES 90 values (anchored against equilibrated gases). The observed difference scaled with the Δ_{47} value of the sample and disappeared when ETH-3 was not considered to correct for scale compression. Moreover, their Δ_{47} (CDES 90) -T calibration for calcite was indistinguishable from the I-CDES calibrations obtained by Jautzy et al. (2020) and Anderson et al. (2021). The Δ_{47}-I-CDES-T relationship of Anderson et al. (2021) integrates data over the calibrations of Breitenbach et al. (2018), Jautzy et al. (2020), Meinicke et al. (2020), and Peral et al. (2018). The calibrations of Jautzy et al. (2020), Anderson et al. (2021) and Meinicke et al. (2020) were made using the Kiel IV and the NU Carb which perform acid digestion at a temperature of 70°C under dropwise addition of phosphoric acid, instead of the 90°C characteristic of the common acid bath setup used by Fiebig et al. (2021). Notably, Δ_{47} (I-CDES) data of Laghetto Basso and Devils Hole calcites made at LSCE using the analytical setup of Peral et al. (2018) agreed with corresponding CDES 90 values made on the same sample material at Goethe University (GU) only if ETH-3 was not considered for the correction of the GU mass spectrometric raw data (Fiebig et al., 2021). GU and LSCE use a very similar methodology (common acid bath, acid digestion at 90°C, GC purification over packed Porapak Q), but the reaction time at GU is set to 30 minutes instead of the 15 minutes used at LSCE (Peral et al., 2018).

In order to test the effect of reaction time for our analytical setup we also reacted unbleached ETH-3 for 10 minutes (ETH-3$_{10min}$) within the last session. The dual clumped isotope composition of the extracted CO_2 is not significantly different from that of unbleached ETH-3 reacted for 30 minutes and nicely aligns along a slope indicative of NO_2 contamination if all data on bleached and unbleached ETH-3 from this session is considered (Fig. 5a). This suggests that reaction time alone is not the sole driving force for the observed NO_2 bias. Notably, least biased Δ_{47} (CDES 90) values on unbleached ETH-3 were obtained in the first two sessions. In these sessions, the filament current was set to 1.5 mA. It was only afterwards that the current was raised to 2.0 mA in order to improve sensitivity. At 2.0 mA, the largest biases in session-mean Δ_{47} (CDES 90) values were obtained for sessions in which the filament blew (Bernecker et al., 2023). It remains unclear how filament current may play a role. Since electron density alone is not expected to change the ionization efficiency of NO_2 relative to CO_2, it might be that the higher temperature of the filament favors preferred ionization of NO_2 over CO_2.

In any case, the experiments of Hu et al. (2019) demonstrated that NO$_2$ formation also proceeds at 70°C. Tagliavento et al. (2023b) noted that Greenland shark dentine, analyzed in 43 replicates, departed by -30 ppm from its predicted equilibrium Δ_{47} value when it was reacted with the Kiel IV setup at 70°C for 30 minutes, using a static Porapak trap at -40°C for gas purification and fixing filament current at 2.0 mA. We also reacted Greenland shark dentine SLGDenA for 90 minutes at a temperature of 90°C using HAL. The obtained data point plots well below the equilibrium line (Fig. 12). Relative to the equilibrium Δ_{47} and Δ_{48} values predicted by the expected body temperature of 1° ± 2°C (Löffler et al., 2019), measured values have an offset of -50 ppm and 165 ppm, respectively, indicating that the Greenland shark dentine might suffer from nitrate contamination (Fig. 12). If so, the Δ_{47} bias of -30 ppm bias obtained by Tagliavento et al. (2023b) may point to the presence of significant amounts of NO$_2$ interferent when reacting at 70°C using the Kiel IV setup.
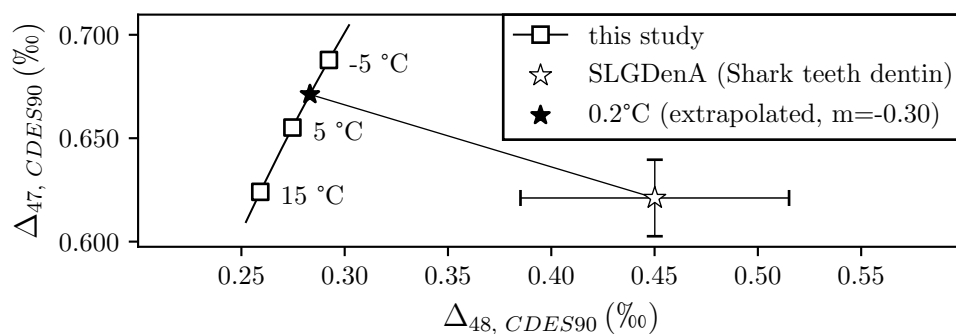
Fig. 12. The dual clumped isotope composition of Greenland shark dentine reacted at 90°C for 90 minutes plots well below the reprocessed calcite equilibrium line. Back-extrapolation of data along a slope of -0.3 yields an apparent body temperature of 0.2°C, in agreement with the range of -1.2 to 3.4°C indicated by logger data (Löffler et al., 2019).

These results imply that the extent of NO$_2$ generation in the presence (of trace amounts) of nitrate may depend on a combination of several factors amongst which are the concentration of nitrate contaminant, trap design, acid temperature, reaction time and filament current/temperature. We recommend that each lab tests their own analytical setup for the effectiveness of NO$_2$ removal, performing sequential bleaching tests on unknown samples with 3 wt-% of NaOCl. The observations of Fiebig et al. (2021) that i) Δ_{47} (CDES 90) values of Laghetto Basso and Devils Hole calcites analyzed at GU are consistent with corresponding I-CDES values made at LSCE and ii) the Δ_{47} (CDES 90) – 1/T calibration of Fiebig et al. (2021) is identical to the I-CDES calibration of Anderson et al. (2021), may imply that NO$_2$ contamination of ETH-3 is only significant in the analytical setup at GU. However, it also needs to be considered that the long-term drift in session-mean Δ_{47} (CDES 90) values at GU is on the

order of -10 to -15 ppm only (Fig. 4d), while the long-term repeatability of Δ_{47} measurements is smaller (8 – 9 ppm; Bernecker et al., 2023; Fiebig et al., 2021). Considering that the long-term repeatability of the Δ_{47} data of Anderson et al. (2021) is 36 ppm, we cannot entirely exclude a potential negative bias in ETH 3-Δ_{47} values went unnoticed in their study, i.e., that it is pure coincidence that the two calibrations are consistent.

Interestingly, our long-term Δ_{47} (CDES 90) values for ETH-1 and ETH-2 confirmed within 1 SE recently assigned Δ_{47}-I-CDES values for these standards (Bernecker et al., 2023). We have also demonstrated in Figure 5a that once- and twice-bleached samples of ETH-3 yielded consistent Δ_{47} (CDES 90) and Δ_{48} (CDES 90) values. We can, therefore, pool over all 34 bleached aliquots of ETH-3 to determine a mean Δ_{47} (CDES 90) value for bleached ETH-3. Pooling over all bleached replicates has been performed in two ways: 1) Anchoring all data relative to equilibrated gases and considering all sessions for variance minimization; 2) Considering the last session exclusively and anchoring raw Δ_{47} data of all bleached ETH-3 aliquots to the nominal I-CDES values of ETH-1 and ETH-2 and nominal Δ_{47} values of equilibrated gases (to account for scale compression). These two approaches yield consistent Δ_{47} (CDES 90) values of 0.6140 ± 0.0023 ‰ (Table 1) and 0.6134 ± 0.0021 ‰ (Supplementary Table S4), respectively, which agree with the recently assigned Δ_{47}-I-CDES value of 0.6132 ± 0.0014 ‰ (n = 264) (all errors represent 1 SE). As a consequence, ETH-3 can easily be replaced by bleached ETH-3 in those labs, in which the analytical setup does not fully suppress NO_2 generation from nitrate and/or enable its quantitative removal.

Sample	$\Delta_{47, CDES90}$	1 SE	$\Delta_{48, CDES90}$	1 SE
ETH-1	**0.2052**	**0.0016**	0.1277	0.0015
ETH-2	**0.2085**	**0.0015**	0.1299	0.0016
ETH-3$_{OXI}$	**0.6132**	**0.0014**	0.2481	0.0071
GU1	0.2254	0.0008	-0.3998	0.0043

Table 2. Mean $\Delta_{47, CDES90}$ and $\Delta_{48, CDES90}$ obtained for ETH-1, ETH-2, ETH-3 and GU1 in Bernasconi et al. (2021) (values in bold, nominal I-CDES values) and this study. $\Delta_{47, CDES90}$ values of Bernasconi et al. (2021) for ETH-1, ETH-2 and ETH-3 were confirmed by Bernecker et al. (2023) (for ETH-1, ETH-2) and in this study (for ETH-3$_{OXI}$, Table 1).

Since our long-term Δ_{47} (CDES 90) values for ETH anchors exactly confirm Δ_{47}-I-CDES assigned for these anchors, use of our long-term values Δ_{48} (CDES 90) values for ETH-1, ETH-2, bleached ETH-3 and GU1 (Table 2) alongside Δ_{47} I-CDES for ETH-1, ETH-2 and ETH-3 might be suitable for reproducible projection of mass spectrometric raw data into dual clumped isotope space. An interlaboratory comparison is necessary to check if reproducibility on unknown samples is achieved based on the Δ_{48} (CDES 90) values listed in Table 2.

769

5 Conclusions

ETH-3, pedogenic carbonates and carbonate slowly precipitated from an equilibrated DIC solution using $Ca(NO_3)_2$ all exhibit excesses in Δ_{48} and depletions in Δ_{47} relative to corresponding aliquots bleached with 3 wt-% NaOCl. The same Δ_{48} enrichment/Δ_{47} depletion patterns are displayed by plasma-ashed echinoderm spicules relative to non-plasma ashed aliquots. The observed deviations follow a unique slope that is characteristic of interferences arising from the presence of sub-ppm quantities of NO_2 isotopologues in the extracted CO_2. The choice of acidification capsules (quartz vs. silver) has no effect on the extent of NO_2 generation. These results support previous findings that NO_2 is generated through the thermal decomposition of HNO_3 which, in turn, is derived from the protonation of NO_3^-. Apparently, in our analytical setup, NO_2 is not effectively removed with cryogenic traps and gas chromatography (packed Porapak Q column, 80-100 mesh, 120 cm, -15°C). We demonstrate that NO_2 interference arising from nitrate becomes insignificant if samples are pre-treated with 3 wt-% NaOCl overnight. The extent of NO_2 generation may depend on analytical setup (e.g., use of static traps vs GC, type of GC column, GC and trap temperatures, etc.) and several other factors such as nitrate concentration inside the carbonate, acid digestion temperature, reaction time, phosphoric acid concentration, filament current and filament age. We, therefore, propose that each lab individually tests the extent of NO_2 generation and effectiveness of NO_2 removal specific to their analytical setup. If NO_2 is determined to have a significant effect in a given laboratory, unknown carbonate samples and ETH-3 should be bleached with 3 wt-% NaOCl in order to avoid any bias in measured Δ_{47} and Δ_{48} values. Because the Δ_{47} (CDES 90) value of bleached ETH-3 agrees with its recently assigned I-CDES value, ETH-3 can be directly replaced by bleached aliquots. With our analytical setup and methodology, nitrate contamination and isobaric NO_2 bias are measurable in pedogenic carbonates, chalk, and, presumably, in bioapatites. Whereas carbon monosulfid (CS) would represent a potent isobaric interferent, we do not have any evidence that the presence of pyrite in carbonate samples compromises Δ_{48} analysis of extracted CO_2.

References

Ameye, L., Hermann, R., Killian, C., Wilt, F., Dubois, P., 1999. Ultrastructural Localization of Proteins Involved in Sea Urchin Biomineralization. *J. Hystochem. Cytochem.* 47, 1189-1200. https://doi.org/10.1177/002215549904700911

Anderson, N.T., Kelson, J.R., Kele, S., Daëron, M., Bonifacie, M., Horita, J., Mackey, T.J., John, C.M., Kluge, T., Petschnig, P., Jost, A.B., Huntington, K.W., Bernasconi, S.M., Bergmann, K.D., 2021. A Unified Clumped Isotope Thermometer Calibration (0.5–1100°C) Using Carbonate-Based Standardization. *Geophys. Res. Lett.* 48, e2020GL092069. https://doi.org/10.1029/2020GL092069.

Bajnai, D., Guo, W., Spötl, C., Coplen, T.B., Methner, K., Löffler, N., Krsnik, E., Gischler, E., Hansen, M., Henkel, D., Price, G.D., Raddatz, J., Scholz, D., Fiebig, J., 2020. Dual clumped isotope thermometry resolves kinetic biases in carbonate formation temperatures. *Nat. Commun.* 11, 4005. https://doi.org/10.1038/s41467-020-17501-0

Bayarjargal, L., Fruhner, C. J., Schrodt, N., Winkler, B., 2018. $CaCO_3$ phase diagram studied with Raman spectroscopy at pressures up to 50 GPa and high temperatures and DFT modeling. *Phys. Earth Planet. Inter.* 281, 31-45. https://doi.org/10.1016/j.pepi.2018.05.002

Bergmann, K.D., Finnegan, S., Creel, R., Eiler, J.M., Hughes, N.C., Popov, L.E., Fischer, W.W., 2018. A paired apatite and calcite clumped isotope thermometry approach to estimating Cambro-Ordovician seawater temperatures. *Geochim. Cosmochim. Acta* 224, 18-41. https://doi.org/10.1016/j.gca.2017.11.015
and isotopic composition

Bernasconi, S.M., Hu, B., Wacker, U., Fiebig, J., Breitenbach, S.F.M., Rutz, T., 2013. Background effects on Faraday collectors in gas-source mass spectrometry and implications for clumped isotope measurements. *Rapid Commun. Mass Spectrom.* 27, 603–612. https://doi.org/10.1002/rcm.6490

Bernasconi, S.M., Müller, I.A., Bergmann, K.D., Breitenbach, S.F.M., Fernandez, A., Hodell, D.A., Jaggi, M., Meckler, A.N., Millan, I., Ziegler, M., 2018. Reducing uncertainties in carbonate clumped isotope analysis through consistent carbonate-based standardization. *Geochem. Geophys. Geosyst.* 19, 2895–2914. https://doi.org/10.1029/2017GC007385

Bernasconi, S.M., Daëron, M., Bergmann, K.D., Bonifacie, M., Meckler, A.N., Affek, H.P., Anderson, N., Bajnai, D., Barkan, E., Beverly, E., Blamart, D., Burgener, L., Calmels, D.,

Chaduteau, C., Clog, M., Davidheiser-Kroll, B., Davies, A., Dux, F., Eiler, J., Elliott, B., Fetrow, A.C., Fiebig, J., Goldberg, S., Hermoso, M., Huntington, K.W., Hyland, E., Ingalls, M., Jaggi, M., John, C.M., Jost, A.B., Katz, S., Kelson, J., Kluge, T., Kocken, I.J., Laskar, A., Leutert, T.J., Liang, D., Lucarelli, J., Mackey, T.J., Mangenot, X., Meinicke, N., Modestou, S.E., Müller, I.A., Murray, S., Neary, A., Packard, N., Passey, B.H., Pelletier, E., Petersen, S., Piasecki, A., Schauer, A., Snell, K.E., Swart, P.K., Tripati, A., Upadhyay, D., Vennemann, T., Winkelstern, I., Yarian, D., Yoshida, N., Zhang, N., 2021. InterCarb: A Community Effort to Improve Interlaboratory Standardization of the Carbonate Clumped Isotope Thermometer Using Carbonate Standards. *Geochem. Geophysi. Geosyst.* 22, e2020GC009588. https://doi.org/10.1029/2020GC009588

Bernecker, M., Hofmann, S., Staudigel, P.T., Davies, A.J., Tagliavento, M., Meijer, N., Ballian, A., Fiebig, J., 2023. A robust methodology for triple (Δ_{47}, Δ_{48}, Δ_{49}) clumped isotope analysis of carbonates. *Chem. Geol.* 642, 121803. https://doi.org/10.1016/j.chemgeo.2023.121803

Bishop, J. L., King, S. J., Lane, M. D., Brown, A. J., Lafuente, B., Hiroi, T., Roberts, R., Swayze, G.A., Lin, J.F., Sánchez Román, M., 2021. Spectral properties of anhydrous carbonates and nitrates. *Earth Space Sci.* 8, e2021EA001844. https://doi.org/10.1029/2021EA001844

Brand, W.A., Assonov, S.S., Coplen, T.B., 2010. Correction for the ^{17}O interference in $\delta(^{13}C)$ measurements when analyzing CO_2 with stable isotope mass spectrometry (IUPAC Technical Report). *Pure Appl. Chem.* 82, 1719-1733. https://doi.org/10.1351/PAC-REP-09-01-05

Breitenbach, S.F.M., Mleneck-Vautravers, M.J., Grauel, A.L., Lo, L., Bernasconi, S.M., Müller, I.A., Rolfe, J., Gázquez, F., Greaves, M., Hodell, D.A., 2018. Coupled Mg/Ca and clumped isotope analyses of foraminifera provide consistent water temperatures. *Geochim. Cosmochim. Acta* 236, 283-296. https://doi.org/10.1016/j.gca.2018.03.010

Daëron, M., 2021. Full propagation of analytical uncertainties in Δ_{47} measurements. *Geochem. Geophys. Geosyst.* 22, e2020GC009592. https://doi.org/10.1029/2020GC009592

Daëron, M., Vermeesch, P. (2024) Omnivariant Generalized Least Squares regression: theory, geochronological applications, and making the case for reconciled Δ_{47} calibrations. *Chem. Geol.* 647, 121881. https://doi.org/10.1016/j.chemgeo.2023.121881

Davies, A.J., John, C.M., 2017. Reducing contamination parameters for clumped isotope analysis: The effect of lowering Porapak^{TM} Q trap temperature to below -50°C. *Rapid Commun. Mass Spectrom*. 31, 1313-1323. https://doi.org/10.1002/rcm.7902

869   Davies, A.J., John, C.M., 2018. The clumped (^{13}C-^{18}O) isotope composition of echinoid

870 calcite: Further evidence for "vital effects" in the clumped isotope proxy. *Geochim.*

871 *Cosmochim. Acta* 245, 172-189. https://doi.org/10.1016/j.gca.2018.07.038

872   Davies, A.J., Guo, W., Bernecker, M., Tagliavento, M., Raddatz, J., Gischler, E., Flögel, S.,

873 Fiebig, J., 2022. Dual clumped isotope thermometry of coral carbonate. *Geochim. Cosmochim.*

874 *Acta* 338, 66–78. https://doi.org/10.1016/j.gca.2022.10.015

875   Davies, A.J., Brand, U., Tagliavento, M., Bitner, M.A., Bajnai, D., Staudigel, P., Bernecker,

876 M., Fiebig, J., 2023. Isotopic disequilibrium in brachiopods disentangled with dual clumped

877 isotope thermometry. *Geochim. Cosmochim. Acta* 359, 135-147.

878 https://doi.org/10.1016/j.gca.2023.08.005

879   Diaz, D., Hahn, D.W., 2020. Raman spectroscopy for detection of ammonium nitrate as an

880 explosive precursor used in improvised explosive devices. *Spectrochim. Acta A Mol. Biomol.*

881 *Spectrosc.* 233, 118204. https://doi.org/10.1016/j.saa.2020.118204

882   Eagle, R.A., Schauble, E.A., Tripati, A.K., Tütken, T., Hulbert, R.C., Eiler, J.M., 2010.

883 Body temperatures of modern and extinct vertebrates from ^{13}C-^{18}O bond abundances in

884 bioapatite. *Proc. Natl. Acad. Sci. U.S.A.* 107, 10377-10382.

885 https://doi.org/10.1073/pnas.0911115107

886   Eiler, J.M., Schauble, E., 2004. ^{18}O^{13}C^{16}O in Earth's atmosphere. *Geochim. Cosmochim.*

887 *Acta* 68, 4767–4777. https://doi.org/10.1016/j.gca.2004.05.035

888   Eiler, J.M., 2011. Paleoclimate reconstruction using carbonate clumped isotope

889 thermometry. *Quatern. Sci. Rev.* 30, 3575-3588.

890 https://doi.org/10.1016/j.quascirev.2011.09.001

891   Fiebig, J., Hofmann, S., Löffler, N., Lüdecke, T., Methner, K., Wacker, U., 2016. Slight

892 pressure imbalances can affect accuracy and precision of dual inlet-based clumped isotope

893 analysis. *Isot. Environ. Health Stud.* 52, 12–28.

894 https://doi.org/10.1080/10256016.2015.1010531

895   Fiebig, J., Bajnai, D., Löffler, N., Methner, K., Krsnik, E., Mulch, A., Hofmann, S., 2019.

896 Combined high-precision Δ_{48} and Δ_{47} analysis of carbonates. *Chem. Geol.* 522, 186–191.

897 https://doi.org/10.1016/j.chemgeo.2019.05.019

898   Fiebig, J., Daëron, M., Bernecker, M., Guo, W., Schneider, G., Boch, R., Bernasconi, S.M.,

899 Jautzy, J., Dietzel, M., 2021. Calibration of the dual clumped isotope thermometer for

900 carbonates. *Geochim. Cosmochim. Acta* 312, 235-256.

901 https://doi.org/10.1016/j.gca.2021.07.012

Gaffey, S.J., Bronnimann, C.E., 1993. Effects of bleaching on organic and mineral phases in biogenic carbonates. *J. Sediment. Petrol.* 63, 752-754.

Ghosh, P., Adkins, J., Affek, H., Balta, B., Guo, W., Schauble, E.A., Schrag, D., Eiler, J.M., 2006. ^{13}C-^{18}O bonds in carbonate minerals: a new kind of paleothermometer. *Geochim. Cosmochim. Acta* 70, 1439–1456. https://doi.org/10.1016/j.gca.2005.11.014

Guo, W., Eiler, J.M., 2007. Temperatures of aqueous alteration and evidence for methane generation on the parent bodies of the CM chondrites. *Geochim. Cosmochim. Acta* 71, 5565-5575. https://doi.org/10.1016/j.gca.2007.07.029

Guo, W., Zhou, C., 2019. Patterns and controls of disequilibrium isotope effects in speleothems: Insights from an isotope-enabled diffusion-reaction model and implications for quantitative thermometry. *Geochim. Cosmochim. Acta* 267, 196–226. https://doi.org/10.1016/j.gca.2019.07.028

Guo W., 2020. Kinetic clumped isotope fractionation in the DIC-H_2O-CO_2 system: Patterns, controls, and implications. *Geochim. Cosmochim. Acta* 268, 230-257. https://doi.org/10.1016/j.gca.2019.07.055

He, B., Olack, G.A., Colman, A.S., 2012. Pressure baseline correction and high-precision CO_2 clumped-isotope (Δ_{47}) measurements in bellows and micro-volume modes. *Rapid Commun. Mass Spectrom.* 26, 2837–2853. https://doi.org/10.1002/rcm.6436

Hetmańczyk, J., Hetmańczyk, Ł., Migdał-Mikuli, A., Mikuli, E., Drużbicki, K., Wesełucha-Birczyńska, A., Proniewicz, L. M., 2009. Vibrations and reorientations of H_2O molecules and NO_3^- anions in $[Ca(H_2O)_4](NO_3)_2$ studied by incoherent inelastic neutron scattering, Raman light scattering, and infrared absorption spectroscopy. *J. Chem. Phys.* 131, 094506. https://doi.org/10.1063/1.3202767

Hu, B., Gao, J., Fan, C., Li, Y., Qin, Y., Zhao, Y., Tian, Y., 2019. Impact of nitrate contamination on the analysis of carbon and oxygen isotopes in carbonate and a low-temperature phosphoric acid digestion approach for online sample preparation. *Rapid Commun. Mass. Spectrom.* 33, 12-20. https://doi.org/10.1002/rcm.8289

Huntington, K.W., Eiler, J.M., Affek, H.P., Guo, W., Bonifacie, M., Yeung, L.Y., Thiagarajan, N., Passey, B., Tripati, A., Daëron, M., Came, R., 2009. Methods and limitations of 'clumped' CO_2 isotope (Δ_{47}) analysis by gas-source isotope ratio mass spectrometry. *J. Mass Spectrom.* 44, 1318-1329. https://doi.org/10.1002/jms.1614

Jautzy, J.J., Savard, M.M., Dhillon, R.S., Bernasconi, S.M., Smirnoff, A., 2020. Clumped isotope temperature calibration for calcite: Bridging theory and experimentation. *Geochem. Perspect. Lett.* 14, 36-41. https://doi.org/10.7185/geochemlet.2021

Keatings, K.W., Holmes, J.A., Heaton, T.H.E., 2006. Effects of pre-treatment on ostracod valve chemistry. *Chem. Geol.* 235, 250–261. https://doi.org/10.1016/j.chemgeo.2006.07.003

Kim, B.K., Jeon, M., Park, A.J., Kim, H.C., Min, J.O., Park, J., Ha, S.Y., 2022. Variability in the Carbon and Nitrogen Uptake Rates of Phytoplankton Associated with Wind Speed and Direction in the Marian Cove, Antarctica. *Front. Mar. Sci.* 9, 887909. https://doi.org/10.3389/fmars.2022.887909

Krul, E.S., 2019. Calculation of Nitrogen-to-Protein Conversion Factors: A Review with a Focus on Soy Protein. *J. Am. Oil Chem. Soc.* 96, 339-364. https://doi.org/10.1002/aocs.12196

Loughney, K. M., Badgley C., 2017. Facies, Environments, and Fossil Preservation in the Barstow Formation, Mojave Desert, California. *Palaios* 32, 396–412. https://doi.org/10.2110/palo.2017.008

Löffler, N., Fiebig, J., Mulch, A., Tütken, T., Schmidt, B.C., Bajnai, D., Conrad, A.C., Wacker, U., Böttcher, M.E., 2019. Refining the temperature dependence of the oxygen and clumped isotopic compositions of structurally bound carbonate in apatite. *Geochim. Cosmochim. Acta* 253, 19-38. https://doi.org/10.1016/j.gca.2019.03.002

Liu, Y. J., Zhu, T., Zhao, D. F., Zhang, Z. F., 2008. Investigation of the hygroscopic properties of $Ca(NO_3)_2$ and internally mixed $Ca(NO_3)_2/CaCO_3$ particles by micro-Raman spectrometry. *Atmos. Chem. Phys.* 8, 7205-7215. https://doi.org/10.5194/acp-8-7205-2008

Meinicke, N., Ho, S.L., Hannisdal, B., Nürnberg, D., Tripati, A., Schiebel, R., Meckler, A.N., 2020. A robust calibration of the clumped isotopes to temperature relationship for foraminifers. *Geochim. Cosmochim. Acta* 270, 160-183. https://doi.org/10.1016/j.gca.2019.11.022

Neumann, C., 2012. The early Maastrichtian (Late Cretaceous) chalk of Rügen. In: Centenary Meeting of the Paläontologische Gesellschaft. Programme, Abstracts, and Field Guides, 24–29 September, 2012, Museum für Naturkunde Berlin, Germany; Editors: Witzmann, Aberhan, pp. 206-210.

Passey, B.H, Levin, N.E., Cerling, T.E., Brown, F.H., Eiler, J.M., 2010. High-temperature environments of human evolution in East Africa based on bond ordering in paleosol carbonates. *Proc. Natl. Acad. Sci. U.S.A*. 107, 11245-11249. https://doi.org/10.1073/pnas.1001824107

Peral, M. Daëron, M., Blamart, D., Bassinot, F., Dewilde, F., Smialkowski, N., Isguder, G., Bonnin, J., Jorissen, F., Kissel, C., Michel, E., Vazquez Riveiros, N., Waelbroeck, C., 2018. Updated calibration of the clumped isotope thermometer in planktonic and benthic foraminifera. *Geochim. Cosmochim. Acta* 239, 1-16. https://doi.org/10.1016/j.gca.2018.07.016

969 Sánchez-Pastor, N., Oehlerich, M., Astilleros, J. M., Kaliwoda, M., Mayr, C. C.,
970 Fernández-Díaz, L., Schmahl, W. W., 2016. Crystallization of ikaite and its pseudomorphic
971 transformation into calcite: Raman spectroscopy evidence. *Geochim. Cosmochim. Acta,* 175,
972 271-281. https://doi.org/10.1016/j.gca.2015.12.006

973 Schlack, T.R., Beal, S.A., Corriveau, E.J., & Clausen, J.L., 2021. Detection limits of
974 trinitrotoluene and ammonium nitrate in soil by Raman spectroscopy. *ACS Omega*, 6, 16316-
975 16323. https://doi.org/10.1021/acsomega.1c00721

976 Snell, K.E., Koch, P.L., Druschke, P., Foreman, B.Z., Eiler, J.M., 2014. High elevation of
977 the "Nevadaplano" during the Late Cretaceous. *Earth Planet. Sci. Lett*. 386, 52-63.
978 https://doi.org/10.1016/j.epsl.2013.10.046

979 Spahr, D., König, J., Bayarjargal, L., Milman, V., Person, M.P., Winkler, B., 2021.
980 Structural, Physical, and Thermodynamic Properties of Aragonitic $Ca_xSr_{1-x}CO_3$ Solid
981 Solutions. *J. Phys. Chem. C* 125, 17474-17481. https://doi.org/10.1021/acs.jpcc.1c04703

982 Staudigel, P.T., Murray, S., Dunham, D.P., Frank, T.D., Fielding, C.R., Swart, P.K., 2018.
983 Cryogenic brines as diagenetic fluids: Reconstructing the diagenetic history of the Victoria
984 Land Basin using clumped isotopes. *Geochim. Cosmochim. Acta*. 224, 154-170.
985 https://doi.org/10.1016/j.gca.2018.01.002

986 Staudigel, P., Davies, A.J., Bernecker, M., Tagliavento, M., van der Lubbe, H.J.L.,
987 Nooitgedacht, C., Looser, N., Bernasconi, S.M., Vonhof, H., Fiebig, J., 2023a. Fingerprinting
988 kinetic isotope effects and diagenetic exchange reactions using fluid inclusion and dual-
989 clumped isotope analysis. *Geochem. Geophys. Geosyst.* 24, e2022GC010766.
990 https://doi.org/10.1029/2022GC010766

991 Staudigel, P., Pederson, C., van der Lubbe, H., Bernecker, M., Tagliavento, M., Davies, A.,
992 Immenhauser, A., Fiebig, J., 2023b. An isotopologue-enabled model (Δ_{47}, Δ_{48}) for describing
993 thermal fluid-carbonate interaction in open and closed diagenetic systems. *Geochem. Geophys.
994 Geosyst.* 24, e2023GC011117. https://doi.org/10.1029/2023GC011117

995 Staudigel, P., Feng, D., Peckmann, J., Bernecker, M., Davies, A., Tagliavento, M., Fiebig,
996 J., 2024. Resolving and correcting for kinetic biases on methane seep paleotemperature using
997 carbonate Δ_{47}/Δ_{48} analysis. *Sci. Adv.*, in press.

998 Tagliavento, M., Davies, A.J., Bernecker, M., Staudigel, P.T., Dawson, R.R., Dietzel, M.,
999 Götschl, K., Guo, W., Schulp, A.S., Therrien, F., Zelenitsky, D.K., Gerdes, A., Müller, W.,
1000 Fiebig, J., 2023a. Evidence for heterothermic endothermy and reptile-like eggshell
1001 mineralization in Troodon, a non-avian maniraptoran theropod. *Proc. Natl. Acad. Sci. U.S.A*.
1002 120, e2213987120. https://doi.org/10.1073/pnas.2213987120

1003   Tagliavento, M., Hofmann, S., Böttcher, M.E., Peltz, M., Fiebig, J., 2023. Clumped isotope

1004   analysis of (bio)apatite using a Kiel IV device in long-integration dual-inlet mode. *Rapid*

1005   *Commun. Mass Spectrom.* 37, e9656. https://doi.org/10.1002/rcm.9656

1006   Wacker, U., Rutz, T., Löffler, N., Conrad, A.C., Tütken, T., Böttcher, M.E., Fiebig, J., 2016.

1007   Clumped isotope thermometry of carbonate-bearing apatite: Revised sample pre-treatment, acid

1008   digestion, and temperature calibration. *Chem. Geol.* 443, 97–110.

1009   https://doi.org/10.1016/j.chemgeo.2016.09.009

1010   Wierzbowski, H., 2007. Effects of pre-treatments and organic matter on oxygen and carbon

1011   isotope analyses of skeletal and inorganic calcium carbonate. *Intern. J. Mass Spectrom.* 268,

1012   16-29. https://doi.org/10.1016/j.ijms.2007.08.002

1013   Zhan, N., Lin, M., Yamada, K., Kano, A., Liu, Q., Yoshida, N., Matsumoto, R., 2020. The

1014   effect of H_2O_2 treatment on stable isotope analysis ($\delta^{13}C$, $\delta^{18}O$ and Δ_{47}) T of various carbonate

1015   minerals. *Chem. Geol.* 532, 119352. https://doi.org/10.1016/j.chemgeo.2019.119352